

Nociceptor-immune interactomes reveal insult-specific immune signatures of pain

Received: 5 June 2023

Accepted: 25 April 2024

Published online: 28 May 2024

 Check for updates

Aakanksha Jain¹, Benjamin M. Gyori^{2,3,4}, Sara Hakim^{1,5}, Ashish Jain⁶, Liang Sun⁶, Veselina Petrova¹, Shamsuddin A. Bhuiyan⁷, Shannon Zhen¹, Qing Wang⁸, Riki Kawaguchi^{8,9}, Samuel Bunga², Daniel G. Taub¹, M. Carmen Ruiz-Cantero¹⁰, Candace Tong-Li¹, Nicholas Andrews¹¹, Masakazu Kotoda¹², William Renthal⁷, Peter K. Sorger^{2,13} & Clifford J. Woolf^{1,5} ✉

Inflammatory pain results from the heightened sensitivity and reduced threshold of nociceptor sensory neurons due to exposure to inflammatory mediators. However, the cellular and transcriptional diversity of immune cell and sensory neuron types makes it challenging to decipher the immune mechanisms underlying pain. Here we used single-cell transcriptomics to determine the immune gene signatures associated with pain development in three skin inflammatory pain models in mice: zymosan injection, skin incision and ultraviolet burn. We found that macrophage and neutrophil recruitment closely mirrored the kinetics of pain development and identified cell-type-specific transcriptional programs associated with pain and its resolution. Using a comprehensive list of potential interactions mediated by receptors, ligands, ion channels and metabolites to generate injury-specific neuroimmune interactomes, we also uncovered that thrombospondin-1 upregulated by immune cells upon injury inhibited nociceptor sensitization. This study lays the groundwork for identifying the neuroimmune axes that modulate pain in diverse disease contexts.

Inflammatory pain is associated with autoimmune diseases, tissue injury and infections. Under healthy circumstances, pain is protective as it is triggered only when specialized sensory neurons, called nociceptors, sense and respond to damaging stimuli such as noxious heat, chemicals or high mechanical force¹. However, during tissue inflammation, inflammatory mediators released from immune cells act on nociceptors to reduce their threshold for activation, resulting in peripheral sensitization, a major driver of pain at the site of inflammation¹. Since this is an immune stimulus-triggered process, immune ligands are an attractive target to alleviate inflammatory pain hypersensitivity. Indeed, nonsteroidal anti-inflammatory drugs are effective against inflammatory pain by inhibiting prostaglandin production; however, chronic nonsteroidal anti-inflammatory drug use can cause serious side effects such as gastric lining corrosion and blood pressure dysregulation, necessitating the identification of new

neuroimmune targets to treat pain². However, due to the large variety and complex temporal dynamics of immune cells in inflamed tissues, our understanding of the immune mechanisms governing peripheral sensitization remains limited. The quality of the immune response is also dictated by the type of insult³. Additionally, sensory neurons in the dorsal root ganglia (DRG) are a heterogeneous population that could react differently to different immune ligands⁴. The resultant inflammatory pain hypersensitivity is, therefore, a cumulative outcome of a large array of ligands produced by various immune cells acting on distinct neuronal populations in an injury-specific manner⁵. In this Resource, to comprehensively map the neuroimmune landscape of inflammatory pain, we decided to characterize how the immune population changes within painful, inflamed tissues in diverse inflammatory pain conditions. We performed a single-cell transcriptomic analysis (single-cell RNA sequencing, scRNA-seq) of skin immune cells at 4, 24

A full list of affiliations appears at the end of the paper. ✉ e-mail: clifford.woolf@childrens.harvard.edu

and 48 h following inflammatory insults with zymosan injection, skin incision and ultraviolet (UV) burn to represent distinct clinical conditions: pathogen invasion, trauma and burn injury. We complemented the immune transcriptomics with a single-nucleus RNA sequencing (snRNA-seq) dataset of DRG neurons using a receptor–ligand database compiled by an automated knowledge assembly tool to annotate pain-related neuroimmune axes⁶. This approach revealed neuroimmune interactions specific to particular inflammatory pain conditions, as well as immune regulators of pain, conserved across diverse injury types and with, therefore, broader therapeutic potential.

Results

Kinetics of immune infiltration correlate with pain development

Hind paw of 8–12-week-old C57BL/6J wild-type mice were subcutaneously injected with 20 μ l of 5 mg ml⁻¹ zymosan in saline (hereafter zymosan model), subjected to 3 mm incision on the plantar surface of the hind paw using a sterile scalpel followed by two to three sutures (hereafter incision model), or exposed to UV irradiation at an intensity of 1 J cm⁻² for 2 min (hereafter UV burn model). Pain hypersensitivity was assessed using the Hargreaves assay, which consists of evaluating the time taken to withdraw the injured paw upon exposure to a heat source, at 4, 24 and 48 h post-injury. Mice subjected to zymosan or skin incision showed a significant heat hypersensitivity within 4 h compared to the pre-injury baseline, which resolved by 24 and 48 h, respectively (Fig. 1a), while significant heat hypersensitivity in the UV burn mice developed later, at 24 h, and was still high at 48 h (Fig. 1a). The time point of peak of hypersensitivity is hereafter referred to as T_{\max} , which is 4 h for zymosan ($T_{\max,Zy}$), 24 h for incision ($T_{\max,In}$) and 48 h for UV burn ($T_{\max,UV}$) injury. The temporal dynamics of hypersensitivity onset and recovery in these inflammatory pain conditions suggested that distinct immune responses might be involved.

To determine if immune responses to injury underlay the kinetics of pain hypersensitivity, we isolated CD45⁺ immune cells 4, 24 and 48 h post-injury from mouse paw skin in all three models and healthy skin from the contralateral (CL) paw at T_{\max} (4, 24 and 48 h for zymosan, incision and UV burn, respectively) and performed scRNA-seq to identify injury-induced gene programs (Extended Data Fig. 1a and Supplementary Table 1). To classify the cell types across all conditions, we integrated the data and performed a t-distributed stochastic neighbor embedding (t-SNE) dimensionality reduction (Fig. 1b). We used singleR for automated cell type detection (Supplementary Table 2). Because a full dataset of immune cells in inflamed skin has not been generated before, we complemented the singleR predictions with specific cluster annotations based on current knowledge of skin immune populations⁷ (Fig. 1b and Extended Data Fig. 1b). From the scRNA-seq data merged from all injuries and time points, we also identified three subsets of dermal macrophages annotated as *Cx3cr1*^{hi} Macs, *Cd163*⁺ Macs and *MHCII*⁺ Macs based on common expression of *Cd64*, *Selenop* and *Mrc1*, and unique expression of *Cx3cr1*, *Cd163* and *H2-Ab1*, respectively (Fig. 1b and Extended Data Fig. 1b), consistent with three transcriptionally distinct subsets of dermal macrophages in healthy skin⁷. We also identified dendritic cells (DCs) and Langerhans cells (*H2-Ab1*, *Cd74* and *Csf1r*), conventional T cells (T_{conv} cells, *Cd3e* and *Trbc1*), regulatory T cells (T_{reg} cells, *Cd3e* and *Foxp3*), gd T cells (*Trdc*), innate lymphoid cells (ILCs) (*Tox*, no *Cd3e*), B cells (*Cd79a* and *Ighm*), natural killer (NK) cells (*Prf1* and *Gzma*), neutrophils (*SI100a9*), mast cells (*Mcpt4*) and basophils (*Hgf* and *Cyp11a1*) (Extended Data Fig. 1b). Two macrophage populations increased at T_{\max} in the zymosan, incision and UV burn paws compared to zymosan_CL, incision_CL and UV burn_CL respectively, and based on their expression of *Ccr2*, we defined them as *Ccr2*⁺ and *Ccr2*⁻ recruited macrophages (recMac) (Fig. 1c). A small keratinocyte and fibroblast cluster was also detected, due to a less than 100% purity of sorted CD45⁺ cells (Extended Data Fig. 1a). Cells from biological replicates showed minimal batch-to-batch variation (Extended Data Fig. 1c). As such,

single-cell transcriptomics of normal and injured skin identified a broad spectrum of functionally diverse resident and infiltrating immune cells.

We then used a scCODA proportionality analysis to determine how the immune population evolved post-injury in relation to pain hypersensitivity kinetics (Supplementary Tables 3–5). Proportions of neutrophils and *Ccr2*⁺ and *Ccr2*⁻ recMac increased significantly 4 h post-zymosan and post-incision compared to CL controls (Fig. 1c,d), while these populations did not increase significantly in UV burn until 48 h compared to UV burn_CL (Fig. 1c,d). This suggested that infiltration of neutrophils and recMac contributed to the development of heat hypersensitivity in each injury model. The change in the proportion of myeloid cells at T_{\max} , identified by the transcriptional profiling, mirrored that obtained by flow cytometry, which identified neutrophils as Ly6c^{int}CD64⁻ and recMac as Ly6c⁺CD64⁺ (Extended Data Fig. 2a,b). NK cells and basophils also increased in zymosan at T_{\max} compared to zymosan_CL, which resolved at 24 h post-injury (Fig. 1c and Supplementary Table 3). NK cell proportions also increased at 4 h post-incision compared to incision_CL and were resolved by $T_{\max,In}$ (Fig. 1c and Supplementary Table 4).

Changes in skin-resident immune populations were observed and depended on the type of injury. *Cd163*⁺ Macs were significantly reduced in zymosan and incision at all time points compared to CL controls (Fig. 1c). Langerhans cells were significantly reduced at $T_{\max,In}$ compared to incision_CL (Fig. 1c and Supplementary Table 4). In UV burn, the proportion of ILCs decreased, while *Cx3cr1*^{hi} Macs, *MHCII*⁺ Macs and DCs increased at $T_{\max,UV}$ compared to UV burn_CL (Fig. 1c and Supplementary Table 5). As such, the infiltration of neutrophils and recMac broadly correlated with pain development across injury types, while changes in the proportions of tissue-resident immune cells were injury specific.

Macrophage transcriptional changes mirror pain hypersensitivity

Next, we investigated injury-induced gene programs in each immune cell type in the three injury conditions. The greatest number of differentially expressed genes compared to CL were found in the dermal macrophage subsets *Cx3cr1*^{hi} Macs and *MHCII*⁺ Macs (Fig. 2a), and the magnitude of this injury-induced transcriptional response peaked at T_{\max} (Fig. 2a), indicating that the kinetics of the injury-triggered transcriptional changes in dermal macrophages mirrored the temporal development of pain hypersensitivity in each injury model. Comparison of differentially expressed genes in *Cx3cr1*^{hi} Macs (Fig. 2b) or *MHCII*⁺ Macs (Fig. 2c) showed significant numbers of genes unique to each injury type, as well as genes differentially expressed in all three injuries at T_{\max} compared to CL. For example, in *Cx3cr1*^{hi} Macs, *Fgl2* and *Ifngr1* were only upregulated at $T_{\max,UV}$ compared to UV burn_CL, *Arg1* and *Ifnar2* were only upregulated in incision compared to incision_CL at $T_{\max,In}$, and *Ccl3*, *Il1a*, *Il6*, *Nfil3* were only upregulated at $T_{\max,Zy}$ compared to zymosan_CL (Fig. 2b). Similarly, in *MHCII*⁺ Macs, *Btf3* and *Fgl2* were specifically induced at $T_{\max,UV}$, *Arg1*, *Ifnar2*, *Irf7* and *Oasl2* were uniquely upregulated at $T_{\max,In}$, while *Hmgb1*, *Mrc1*, *Cd68* and *Trem2* were downregulated at $T_{\max,Zy}$ compared to the respective CL controls (Fig. 2c). This analysis revealed insights into injury-specific macrophage signatures associated with pain hypersensitivity, with upregulation of inflammatory genes and suppression of phagocytic genes in zymosan and upregulation of interferon-responsive genes in incision.

We then analyzed the set of genes upregulated in *Cx3cr1*^{hi} Macs at $T_{\max,UV}$, $T_{\max,In}$ and $T_{\max,Zy}$ compared to their respective CLs (Fig. 2d). These included genes such as *Thbs1*, *Il1b*, *Chil3*, *Fn1*, *Spp1*, *Ptgs2*, *Btg1*, *Map4k4*, *Hif1a*, *Arg2* and *Ifitm3* (Fig. 2d). *Thbs1*, *Fn1*, *Hif1a*, *Btg1* and *Map4k4* were commonly upregulated in *MHCII*⁺ Macs at $T_{\max,Zy}$, $T_{\max,In}$ and $T_{\max,UV}$ compared to CL (Fig. 2d). At $T_{\max,Zy}$, $T_{\max,In}$ and $T_{\max,UV}$, *Ccr2*⁻ recMac upregulated *Thbs1* and *Hif1a*, *Ccr2*⁺ recMac upregulated *Thbs1*, *Hif1a* and *Arg2*, while *Cd163*⁺ Macs upregulated *Thbs1*, *Il1b*, *Hif1a* and *Morbid* (Extended Data Fig. 3). *Thbs1* was commonly upregulated

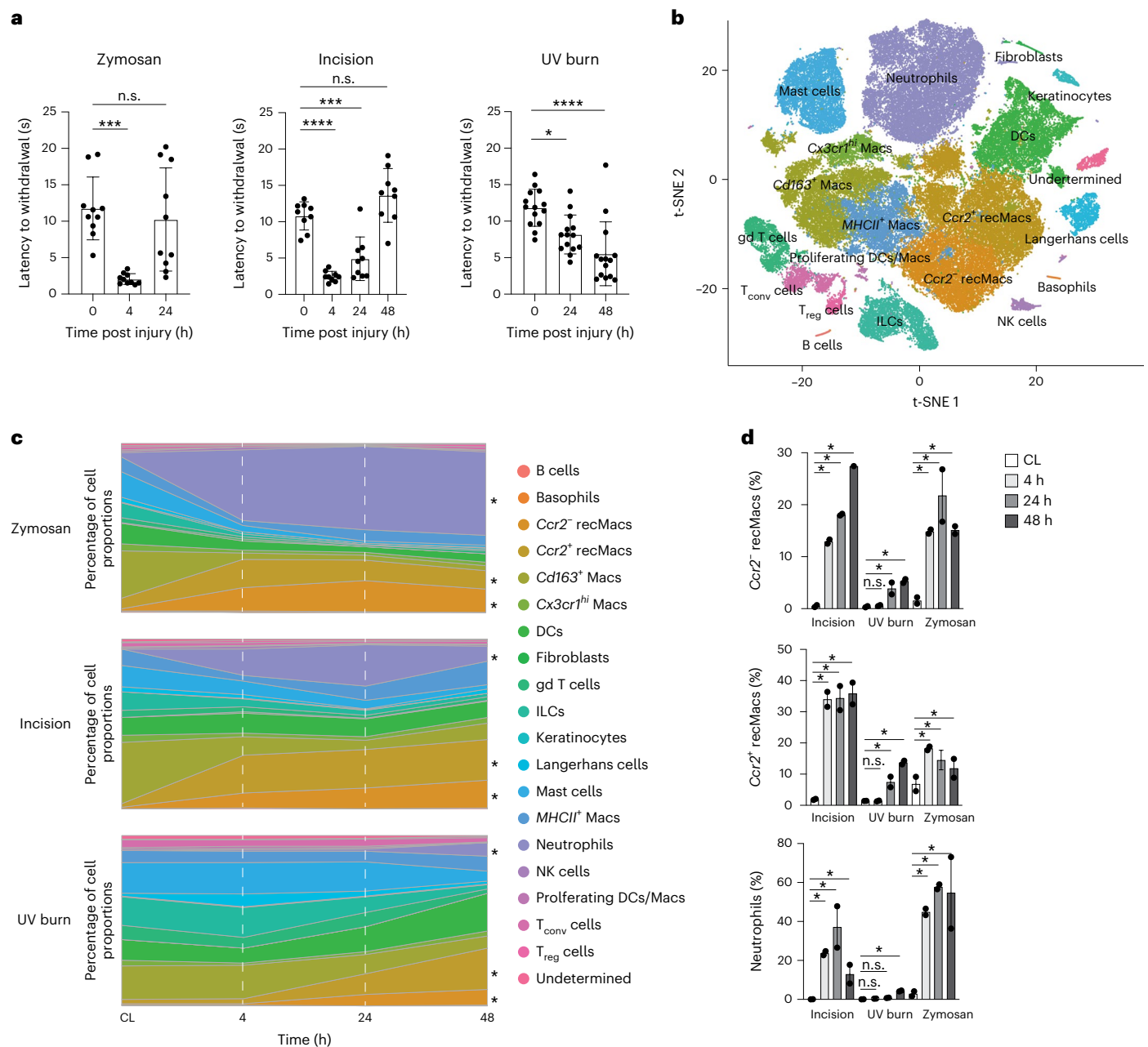


Fig. 1 | Kinetics of immune infiltration correlate with pain development.

a, Heat hypersensitivity in inflamed paws measured by the latency to react in the Hargreaves assay before and 4, 24 and 48 h after zymosan injection ($n = 9$, male 4, female 5), incision ($n = 9$, male 4, female 5), UV burn ($n = 14$, male 5, female 9) in the paws of wild-type (WT) mice. Data are represented as mean value \pm s.e.m. P values calculated using one-way ANOVA, Tukey's multiple comparison test; 8–12-week-old mice were used. **b**, t-SNE plot of scRNA-seq data of hematopoietic CD45⁺ cells-enriched skin from WT mice integrated from all samples. This comprises zymosan injection, incision and UV burn at 4 h, 24 h and 48 h post-injury

and control skin from the CL paws at 4 h (zymosan), 24 h (incision) and 48 h (UV burn). **c**, Stacked area plot of mean proportions of immune cell types at 4 h, 24 h and 48 h in zymosan injection, incision and UV burn and CL healthy skin as in **b**. *Ccr2⁺* recMacs, *Ccr2⁻* recMacs and neutrophils were significantly changed following injury and are marked with an asterisk. **d**, Proportions of *Ccr2⁺* recMacs, *Ccr2⁻* recMacs and neutrophils at 4 h, 24 h and 48 h in zymosan, incision and UV burn injury. *Significant change in cell proportions compared to CL based on scCODA analysis. n.s., no statistically significant change in proportions of the cell type based on scCODA analysis (Methods).

in DCs, gd T cells, T_{conv} cells and ILCs at T_{\max} in all three injury models (Extended Data Fig. 3). *Thbs1* (encoding the secreted protein TSP-1) and *Hif1a* (encoding the transcription factor Hif1a) could therefore be genes strongly associated with pain hypersensitivity. DCs also showed upregulation of interferon genes such as *Ifitm1*, *Ifitm2* and *Ifitm3* at $T_{\max,Zy}$, $T_{\max,In}$ and $T_{\max,UV}$. *Ifitm2* was also upregulated in mast cells at T_{\max} in all injuries (Extended Data Fig. 3).

Among the genes downregulated at T_{\max} in all injuries, transcription factors encoding genes, including *Klf6*, *Atf3*, *Btg2*, *Klf4*, *Jun* and

Fos were suppressed in *Cx3cr1^{hi}* Macs at T_{\max} compared to CL (Fig. 2e). *Klf6*, *Irf4*, *Atf3* and *Fosb* were downregulated in *MHCII⁺* Macs at $T_{\max,Zy}$, $T_{\max,In}$ and $T_{\max,UV}$ compared to CL (Fig. 2e). Several genes associated with anti-inflammatory macrophage program, including *Cl1qa*, *Cl1qb*, *Cl1qc*, *Selenop* and *Cd36*, were also suppressed in both *Cx3cr1^{hi}* and *MHCII⁺* Macs at $T_{\max,Zy}$, $T_{\max,In}$ and $T_{\max,UV}$ compared to CL (Fig. 2e). *Fosb* was downregulated in *Ccr2⁻* and *Ccr2⁺* recMacs, *Cd163⁺* Macs and DCs (Extended Data Fig. 4), while mast cells downregulated other CREB signaling targets, including *Nr4a1* and *Jun* (Extended Data Fig. 4) at

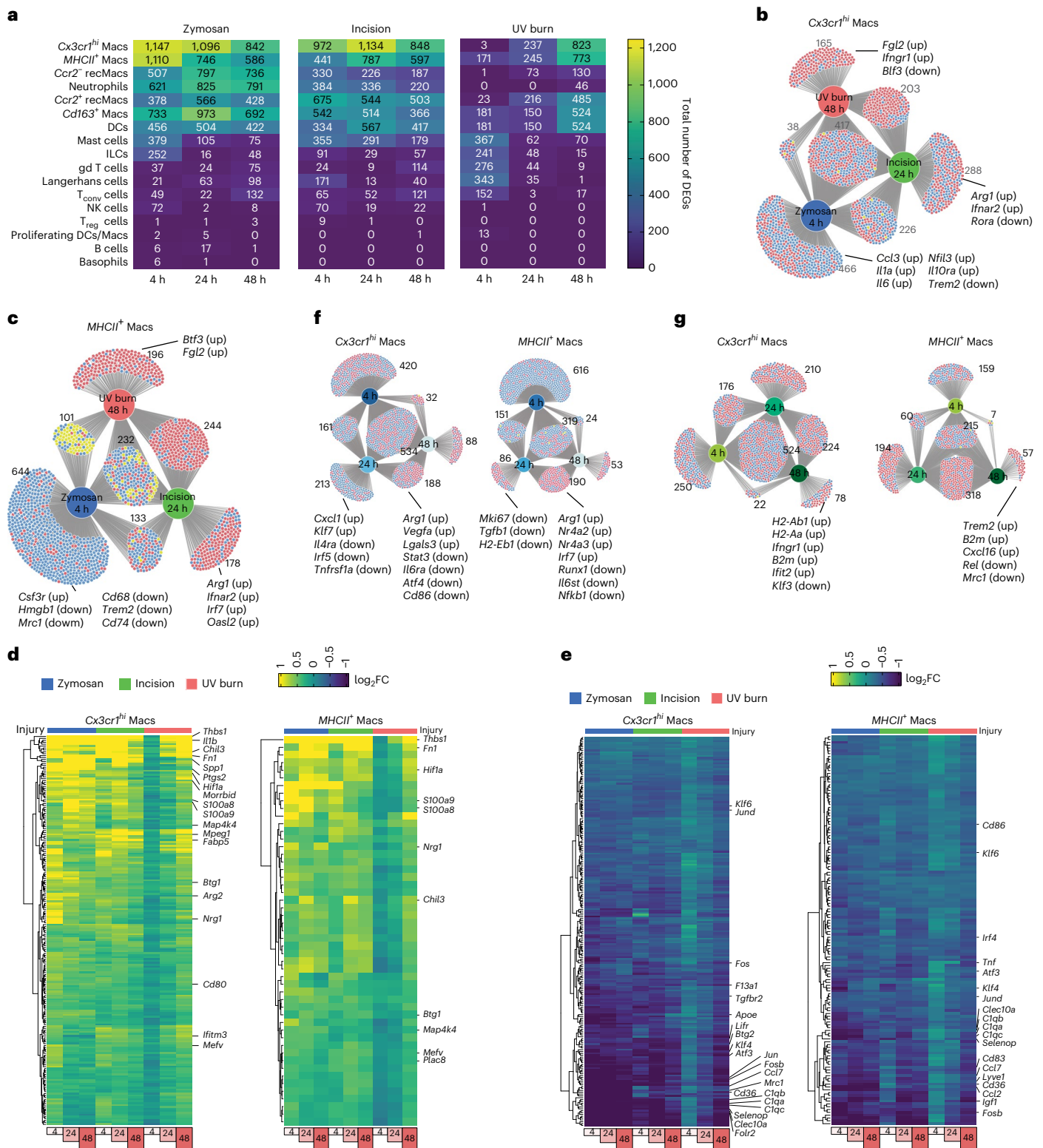


Fig. 2 | Macrophage transcriptional changes mirror pain hypersensitivity.

a, Heatmaps showing the total number of differentially expressed genes (upregulated and downregulated combined) compared to CL in each immune cell type. For differentially expressed genes (DEGs), \log_2FC threshold of 0.25 and min.pct of 0.1 was applied. **b,c**, DiVenn plots showing the overlap of DEGs in different injuries at T_{max} (zymosan at 4 h, incision at 24 h and UV burn at 48 h) compared to CL in *Cx3cr1^{hi}* Macs (**b**) and *MHCII⁺* Macs (**c**). **d,e**, Heatmaps showing the \log_2FC of the upregulated DEGs common in zymosan at 4 h, incision at 24 h

and UV burn at 48 h compared to CL controls in *Cx3cr1^{hi}* Macs (**d**) and *MHCII⁺* Macs (**e**). **f**, DiVenn plots showing the overlap of DEGs in zymosan at different time points of 4 h, 24 h and 48 h compared to CL in *Cx3cr1^{hi}* Macs and *MHCII⁺* Macs. **g**, DiVenn plots showing the overlap of DEGs in incision at different time points of 4 h, 24 h and 48 h compared to CL in *Cx3cr1^{hi}* Macs and *MHCII⁺* Macs. In **b**, **g** and **h**, the red circle denotes upregulated, the blue circles denote downregulated and the yellow circle denotes divergent regulated genes.

$T_{\max,Zy}$, $T_{\max,In}$ and $T_{\max,UV}$. Similar to $Cx3cr1^{hi}$ Macs and $MHCII^+$ Macs, $Ccr2^-$ and $Ccr2^+$ recMacS downregulated $Clqa$, $Clqb$ and $Clqc$ at T_{\max} in all injuries compared to CL (Extended Data Fig. 4). Genes associated with antigen presentation, including $H2-Ab1$, $H2-Eb1$, $H2-Aa$ and $Cd74$, were also suppressed in $Ccr2^-$ and $Ccr2^+$ recMacS (Extended Data Fig. 4), suggesting suppression of genes regulated by CREB signaling or associated with the antigen presentation machinery associated with pain hypersensitivity.

Finally, we asked which gene programs were associated with pain resolution in zymosan and incision injuries by analyzing the transcriptional program unique to the pain-resolving time points (hereafter T_{res}), which was 24 h post-injury in zymosan ($T_{res,Zy}$) and 48 h post-injury in incision ($T_{res,In}$) compared to CL controls. At $T_{res,Zy}$, $Cx3cr1^{hi}$ Macs induced tissue repair genes, including $Arg1$, $Vegfa$ and $Lgla3$, and suppressed $Il4ra$, $Il6ra$, $Stat3$ and $Irf5$ (Fig. 2f). Similarly, $MHCII^+$ Macs showed upregulation of $Arg1$ and suppression of $Il6st$, $Nfkb1$ and $Runx1$ at $T_{res,Zy}$ (Fig. 2f). $Trem2$ and gene associated with antigen presentation ($H2-Ab1$ and $B2m$) were upregulated at $T_{res,In}$ in $MHCII^+$ Macs and $Cx3cr1^{hi}$ Macs, respectively (Fig. 2g), indicating that pain resolution was accompanied by suppression of pain-inducing gene programs and induction of pain-resolving gene signatures.

DRG neurons show subtype-specific receptor expression profiles

To investigate whether DRG neurons expressed receptors that could enable interactions with immune cells, we utilized a published snRNA-seq transcriptomic dataset⁴ from DRG of 8–12-week-old healthy C57BL/6J wild-type male and female mice. DRG neurons do not exhibit transcriptional changes in response to acute inflammatory injury⁴; therefore, we complemented the healthy DRG transcriptome with immune cell transcriptomes in the zymosan, incision and UV burn inflammatory models at all time points. This consists of nine subsets of sensory neurons, including $Tac1^+Gpx3^+$ peptidergic type 1 neurons (PEP1), $Tac1^+Gpx3^-$ peptidergic type 2 neurons (PEP2), $Mrgprd^+$ nonpeptidergic neurons (NP), Sst^+ somatostatin neurons (SST), $Fam19a4^+Th^+c$ fiber low threshold mechanoreceptors (cLTMR1), $Nefh^+Pvalb^-$ neurons (NF1), $Nefh^+Pvalb^+$ neurons (NF2), $Nefh^+Cadps2^+$ neurons (NF3) and $Fam19a4^+Th^{lo}$ putative cLTMR (p_cLTMR2) (Extended Data Fig. 5a). These subsets are functionally distinct, with PEP, PEP2 and NP neurons activated in response to high-intensity mechanical or thermal stimuli, and SST neurons in response to itch. NF1, NF2 and NF3 are low-threshold mechanoreceptors⁸, while the precise function of cLTMR1 and p_cLTMR2 is not well defined (cLTMRs may be involved in mechanical pain)^{9,10}. We performed a differential expression analysis in the DRG neurons of genes encoding proteins considered receptors to understand the ability of different DRG neurons to respond to external stimuli (Supplementary Data File 1). The receptor genes were obtained from the CellPhoneDB database (also used for interactome analyses) (Supplementary Data File 1). This analysis showed that unique repertoires of receptors were expressed in different subsets of sensory neurons (Fig. 3). Subset-specific receptor expression profiles were observed in DRG neurons from both female (Fig. 3) and male (Extended Data Fig. 5b) mice. Many genes expressed in a subtype-specific manner encoded immune receptors (Fig. 3). For example, $Ifngr2$ (encodes the receptor for type I cytokine interferon- γ (IFN γ)), was enriched in cLTMR neurons (Extended Data Fig. 5c), suggesting these neurons preferentially responded to IFN γ -producing cells, such as CD8⁺ T cells and NK cells, which are mediators of anti-viral and anti-tumor immunity. Expression of Kit (encodes KIT, a receptor for KITLG, which potentiates mast cell-mediated allergic inflammation)¹¹, was observed only in PEP1 neurons (Extended Data Fig. 5c), suggesting these neurons amplify allergic immunity^{12,13} and that Kit signaling might sense allergic immune reactions. $Osmr$, which encodes the receptor for the oncostatin M ligand (OSM), was specifically expressed by SST neurons (Extended Data Fig. 5c), consistent with their role in OSM-mediated pruritus¹⁴.

A small proportion of cLTMR1 neurons were enriched in the expression of $Tnfrsf11a$, which encodes RANK, a receptor for the TNF family member RANKL (encoded by $Tnfrsf11$; Extended Data Fig. 5c). Expression of RANK in cLTMR1 neurons pointed to a potential role for neuronal intrinsic RANK signaling in pain¹⁵. Genes encoding several receptors traditionally studied in immune cells, such as $Cd44$ (encoding CD44) and $SIpr1$ (encoding sphingosine-1-phosphate receptor 1), which mediate immune cell trafficking, were also expressed by DRG neurons (Extended Data Fig. 5c). While $Cd44$ was broadly expressed by DRG neurons, $SIpr1$ was highly expressed in SST neurons (Extended Data Fig. 5c), suggesting subset-specific receptor distribution. The differential expression of receptors for immune ligands by DRG neurons showed that different sensory neuron types can distinguish distinct immune cues.

Macrophages are the strongest interactors of sensory neurons

To identify the full spectrum of possible interactions between immune cells and neurons, we used INDRA (integrated network and dynamical reasoning assembler) to assemble a systematic interaction knowledge base (interactome). INDRA builds a knowledge base from a variety of cell-to-cell interaction databases and through text mining of the scientific literature and combines duplicate and overlapping mentions of the same mechanism in a standardized format known as INDRA statements (Fig. 4a)^{6,16}. INDRA standardized the names of genes and proteins to Human Genome Organization Gene Nomenclature (HUGO symbols), which was used for defining interactomes. We included three possible modalities of crosstalk between cell types in the interactome: ligands secreted or expressed on the surface of immune cells that physically interacted with cell surface receptors expressed on neurons (for example, the cytokine IL-6 interacting with its cognate receptor IL-6ST); metabolites whose production and secretion was controlled by enzymes in immune cells and could interact with cell surface receptors on neurons, creating indirect interactions between immune cell enzymes and neuronal receptors (such as the interaction between enzyme PTGS2, which controls production of prostaglandin E2, with the PTGER4 receptor); and proteins or metabolites secreted by immune cells that directly or indirectly interacted with ion channels expressed on the surface of neurons (for example, the interactome of the growth factor NGF with the ion channel TRPV1) (Extended Data Fig. 6a). We first identified a set of proteins considered to be ligands, receptors, enzymes or ion channels to include in the interactome, based on the following datasets: to identify the ligand and receptor proteins, we used the CellPhoneDB database¹⁷ (for each interaction, one interactor was classified as receptor and the other as ligand, based on a set of consensus direction information standardized from multiple sources by OmniPath, which aggregates multiple cell-to-cell interaction databases^{18,19} (Methods)); the enzyme list was constructed on the basis of the ExPASy Enzyme database²⁰, which captures human proteins with enzymatic activity, after excluding kinases and phosphatases as intermediaries in signaling pathways not likely to be directly involved in intercellular interactions; finally, for ion channels, we used a list curated by the NIH Illuminating the Druggable Genome program (<https://druggablegenome.net/>). Together, these resources yielded 941 receptors (Supplementary Data File 1), 560 ligands (Supplementary Data File 2), 2,881 enzymes (Supplementary Data File 3) and 293 ion channels (Supplementary Data File 4).

We used these gene sets to assemble three potential interaction modalities. Ligand–receptor interactions were obtained from OmniPath, then aligned with text mining and structured knowledge evidence collected by INDRA to obtain 2,827 distinct interactions (Fig. 4c). We used the Pathway Commons database to identify products controlled by each enzyme and INDRA to find interactions between these products and receptors²¹, which created 6,868 total interactions between an enzyme's product and a receptor (Fig. 4b and Supplementary Data File 5), while maintaining the underlying relationships between enzymes, products and receptors, which ensured

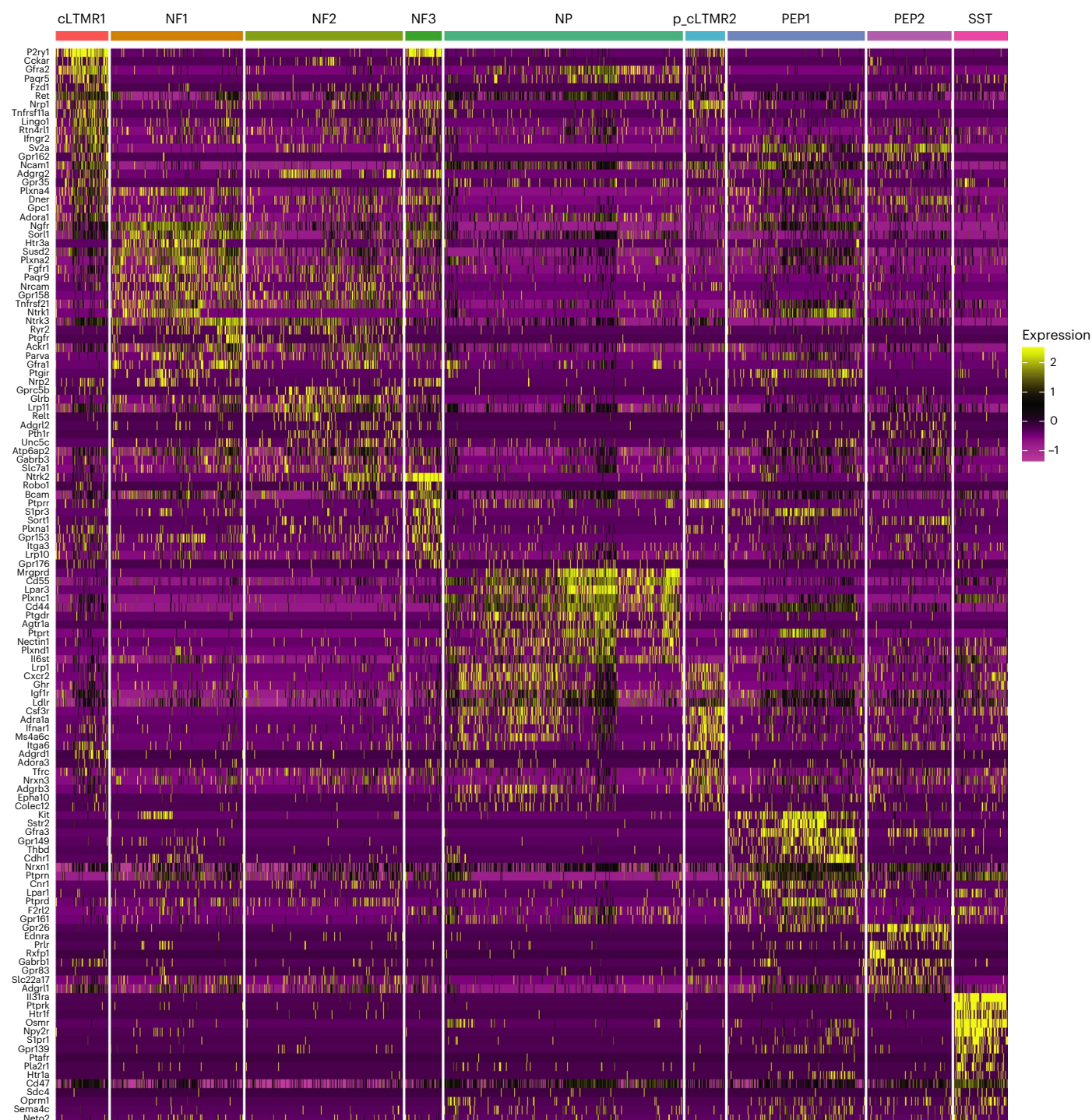


Fig. 3 | DRG neurons have subtype-specific receptor expression profiles. FindMarker analysis of receptor genes expressed by sensory neurons isolated from DRG in female mice based on snRNA-seq data, from ref. 4. Heatmaps show significantly (adjusted $P < 0.05$) differentially expressed receptor genes in neurons with \log_2FC of 0.5 and min.pct of 0.25.

that each interaction was traceable to the evidence from which it was derived (Extended Data Fig. 6b). Finally, we used INDRA to find direct or indirect effects on ion channels involving protein ligands or enzyme products, which added 177 interactions (Fig. 4b). In total, the final interactome contained 9,872 unique interactions (Fig. 4b and Supplementary Data File 6).

Next, we mapped human genes in the INDRA interactome to mouse genes using ortholog mappings made available by HGNC, so the INDRA interactome can be applied to mouse skin immune scRNA-seq and DRG

neuron snRNA-seq data. We complemented each immune scRNA-seq dataset for zymosan, incision and UV burn at 4, 24 and 48 h and CL conditions with snRNA-seq from steady-state DRG neurons⁴ and used CellChat to identify statistically significant interactions between each immune and neuronal cell type²² (Extended Data Fig. 6c). We focused primarily on interactions between immune cells as the source and neurons as receivers (Extended Data Fig. 7), as these are likely to modulate inflammatory pain. *Ccr2*⁺ and *Ccr2*⁻ recMacs and dermal macrophages (*Cx3cr1*^{hi} Macs, *MHCII*⁺ Macs and *Cd163*⁺ Macs) showed the highest

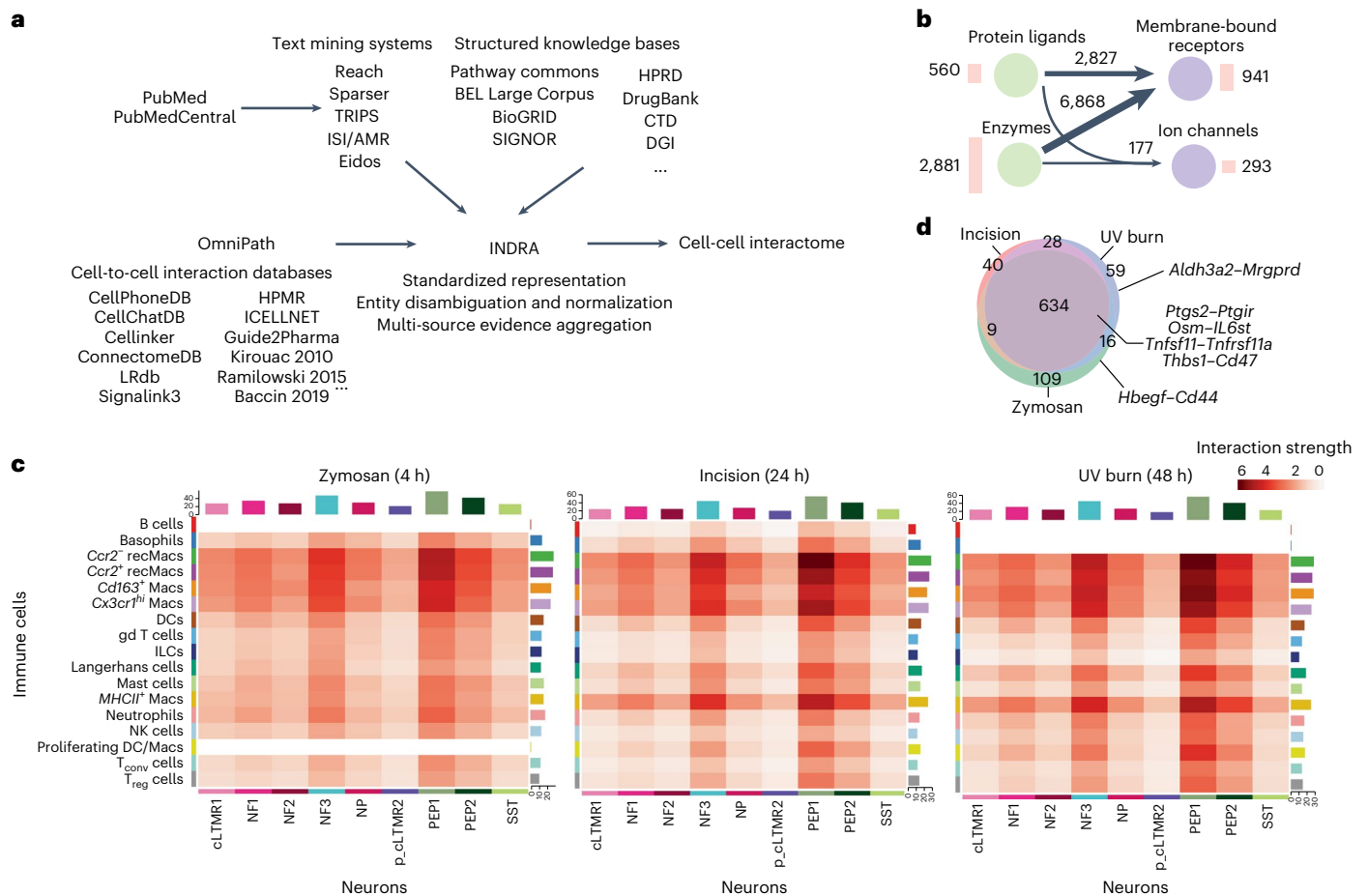


Fig. 4 | Macrophages are the strongest interactors of sensory neurons. a, An overview of the computational pipeline in which INDRA processes publications through multiple text mining systems and combines their output with structured knowledge bases integrated with INDRA directly, as well as the content of cell-to-cell interaction databases obtained via OmniPath to create an assembled cell-cell interactome. **b**, Summary of the modalities of the interactome derived from INDRA. Circles represent types of proteins: ligands, enzymes, membrane-bound receptors and ion channels. Numbers next to the circle represent

protein types in the interactome. Arrows between circles show the number of distinct interactions among the corresponding protein type, with thicker arrows corresponding to a larger number of interactions. **c**, A heatmap of the interaction strength between immune cells (senders) and neurons (receivers) calculated for zymosan, incision and UV burn at T_{max} . Color saturation represents the communication probability between the senders and receivers calculated by CellChat. **d**, Venn diagram depicting the number of shared and unique significant neuroimmune interactions for zymosan, incision and UV burn at T_{max} .

interaction strength with DRG neurons in all three conditions at all time points (Extended Data Fig. 7). The DRG neurons PEP1, PEP2 and NF3 were the strongest interactors with immune cells across all immune cell types (Fig. 4c and Extended Data Fig. 7). The interactomes of incision_CL and UV burn_CL were similar to each other, with no interactions predicted between neutrophils and neurons. However, zymosan_CL showed interactions between neutrophils and DRG neurons (Extended Data Fig. 7), which could be due to zymosan leaking into the circulation and increasing neutrophils recruitment into healthy CL paw skin. We further analyzed a network of bidirectional interactions between immune and neuronal cell types at $T_{max,Zy}$ (Supplementary Data File 7), $T_{max,In}$ (Supplementary Data File 8) and $T_{max,UV}$ (Supplementary Data File 9). The strength of the interaction between gd T cells or ILCs and neurons was reduced at T_{max} in all injuries compared to CL (Extended Data Fig. 7). The majority of neuroimmune interactions between immune cells (source) and neurons (receiver) were shared in all injuries at T_{max} (Fig. 4d and Extended Data Fig. 6d). This included *Ptgs2-Ptgir* (*Ptgs2* encodes prostaglandin synthase 2 (COX-2), the target of nonsteroidal anti-inflammatory drugs²²), *Osm* (encoding the immune ligand oncostatin M)–*Il6st* (encoding the IL-6 receptor family protein, gp130), *Tnfsf11-Tnfrsf11a* and *Thbs1* (encoding secreted thrombospondin-1, TSP-1)–*Cd47* (encoding the receptor CD47) (Fig. 4d). The cell types

mediating these interactions, however, were dependent on the injury type. The cell pairs *Ccr2*⁺ recMacs–PEP1, *Ccr2*⁺ recMacs–PEP1, *Cd163*⁺ Macs–PEP2, *Cx3cr1*^{hi} Macs–PEP2 and *MHCII*⁺ Macs–PEP2 were predicted to mediate the *Ptgs2-Ptgir* interaction at $T_{max,Zy}$ (Extended Data Fig. 6e), while the cell pairs *MHCII*⁺ Macs–PEP2 and the cell pairs *Cd163*⁺ Macs–PEP2 and *MHCII*⁺ Macs–PEP2 did not show *Ptgs2-Ptgir* interactions at $T_{max,Zy}$ or $T_{max,UV}$, respectively (Extended Data Fig. 6e). A *Osm-Il6st* interaction was predicted to be mediated by *Ccr2*⁺ recMacs, *Ccr2*⁺ recMacs, *Cd163*⁺ Macs, *Cx3cr1*^{hi} Macs, *MHCII*⁺ Macs and cLTMR1, NP, PEP1 and PEP2 neurons at $T_{max,Zy}$ (Extended Data Fig. 6e), but not by *Cx3cr1*^{hi} Macs at $T_{max,In}$ and at $T_{max,UV}$ (Extended Data Fig. 6e). A *Thbs1-Cd47* interaction was predicted between all macrophage types and cLTMR1, NF3, NP, PEP1 and PEP2 neurons at $T_{max,In}$ and at $T_{max,UV}$ (Extended Data Fig. 6e). At $T_{max,Zy}$, all macrophage subsets except *Cd163*⁺ Macs mediated *Thbs1-Cd47* interactions. *Tnfsf11-Tnfrsf11a* interaction was predicted to be mediated by *T*_{conv} cells and cLTMR1 neurons in all three injuries at T_{max} (Extended Data Fig. 6e).

The analysis also predicted interactions specific to each inflammatory pain model (Extended Data Fig. 6d). Interactions between *Hbegf* (encoding an inducer of mechanical hypersensitivity) in *Ccr2*⁺ recMacs and *Cx3cr1*^{hi} Macs, and *Cd44* in cLTMR1, NP, PEP1 and PEP2 neurons was uniquely found at $T_{max,Zy}$ (Extended Data Fig. 6e). Interactions between

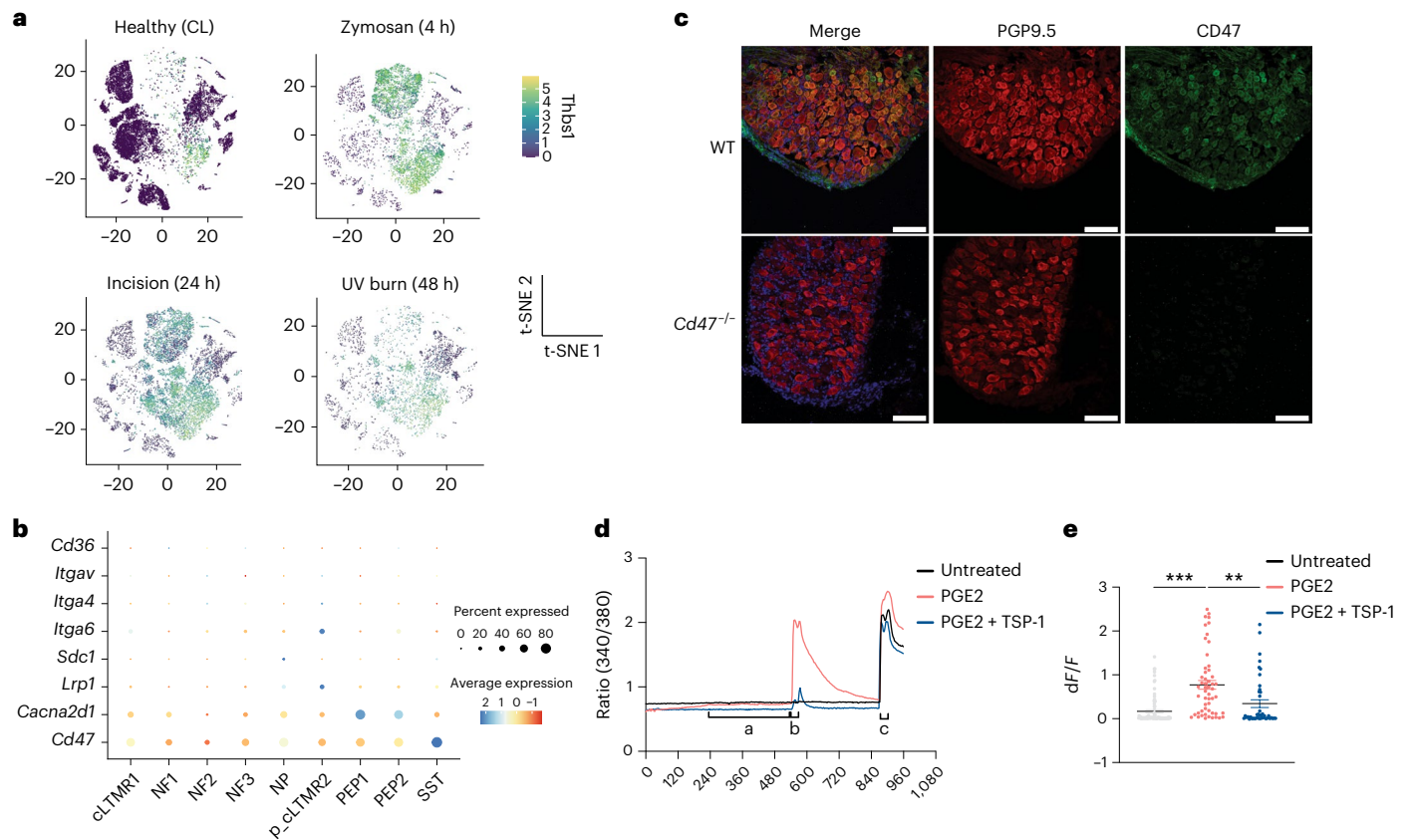


Fig. 5 | TSP-1 inhibits PGE2-mediated nociceptor sensitization. **a**, t-SNE plot of normalized *Thbs1* expression in immune cells from healthy (CL) and inflamed skin following zymosan, incision and UV burn injury at T_{\max} . **b**, Dot plot showing the expression of TSP-1 receptors (*Cd47*, *Cacna2d1*, *Lrp1*, *Sdc1*, *Itga6*, *Itga4*, *Itgav* and *Cd36*) in DRG neuron subtypes (cLTMR1, NF1, NF2, NF3, NP, p_cLTMR2, PEP1 and PEP2) in wild-type (WT) healthy mouse lumbar DRG⁺. **c**, The expression of CD47 on frozen wild-type or *Cd47*^{-/-} DRG neuron sections stained with PGP9.5. Scale bar, 100 μ m. Representative of two independent experiments. **d**, Fura-2-based calcium imaging in cultured sensory neurons from DRG obtained from WT male mice treated with SES, 1 μ M PGE2 or 1 μ M PGE2 + 200 ng ml⁻¹ TSP-1 for 7 min, followed immediately by 100 nM capsaicin, 100 nM capsaicin + 1 μ M PGE2 or 100 nM capsaicin + 1 μ M PGE2 + 200 ng ml⁻¹ TSP-1, respectively for 30 s,

a 5 min SES wash and treatment with 1 μ M capsaicin for 30 s. SES was used as the recording solution. Treatments were applied during live imaging using a gravity-based perfusion system. Frames were captured every 3 s. Intensity traces of ratio of 340/380 are plotted. **e**, dF/F calculated as $(F_1 - F_0)/F_0$, where F_1 is the peak response within 40 s of treatment with 100 nM capsaicin and F_0 is the average of 10 s before the PGE2-treatment time point. SES, $n = 80$; PGE2, $n = 55$; PGE2 + TSP, $n = 42$. All TRPV1⁺ neurons are from one experiment consisting of three separate recordings for each condition. Data are represented as mean value \pm s.e.m. Unpaired two-tailed *t*-test was performed. $P < 0.05$ was considered significant. An individual dot represents a neuron that was included in the analysis. Data are representative of three independent experiments.

Aldh3a2, which encodes aldehyde dehydrogenase 3, in T_{reg} cells and *Mrgprd* occurred at $T_{\text{max,UV}}$ (Fig. 4d and Extended Data Fig. 6d,e). *Aldh3a2* controls the production of beta-alanine, an itch inducer²³, and this interaction might underlie UV burn-specific mechanisms of itch (Extended Data Fig. 6e). Thus, interactome analysis predicted known pain and itch pathways such as *Ptgs2*-*Ptgir*, *Osm*-*Il6st*, *Tnfsf11*-*Tnfrsf11a* and *Aldh3a2*-*Mrgprd*, and previously unappreciated neuroimmune interactions in the periphery, including *Thbs1*-*Cd47*.

TSP-1 inhibits PGE2-mediated nociceptor sensitization

TSP-1 interacts with CD47 on platelets to trigger Gi-coupled GPCR signaling, which attenuates the activation of the PKA kinase^{24,25}. Expression of *Thbs1* increased in neutrophils, *Ccr2*⁺ recMacs, *Ccr2*⁻ recMacs, *MHCI*⁺ Macs, *Cx3cr1*^{hi} Macs, DCs, ILCs and T_{conv} cells at $T_{\text{max,Zy}}$, $T_{\text{max,In}}$ and $T_{\text{max,UV}}$ (Fig. 5a). Expression of *Thbs1* correlated with the expression of *Ptgs2* across all cells in all three injuries at all time points and mirrored the development of pain hypersensitivity in all injuries (Extended Data Fig. 8a), suggesting that neurons were concurrently exposed to both TSP-1 and pain-sensitizing molecules like prostaglandin E2. Expression of *Cd47* in mouse DRG neurons was higher than other TSP-1 receptors²⁶ (Fig. 5b) and was enriched in DRG neurons that drive pain

or itch (PEP1, PEP2, NP and SST) compared to low-threshold mechanoreceptors (NF1, NF2 and NF3) (Fig. 5b), indicating a potential role for CD47 signaling in regulating nociception. We also confirmed that CD47 was expressed on mouse DRG neurons (Fig. 5c). In nociceptors, activation of PKA triggers several sensitization pathways by direct phosphorylation of TRPV1 and Nav1.8 channels, which lowers channel activation thresholds²⁷⁻²⁹. To test whether TSP-1 signaled through CD47 to modify PKA-mediated TRPV1 sensitization in DRG neurons, we used a capsaicin-induced sensitization assay in cultured mouse DRG neurons. Capsaicin-responsive, TRPV1⁺ nociceptor neurons were exposed to PGE2 as a sensitizing agent, and intracellular calcium levels were measured using the calcium-sensitive fluorescent dye, Fura-2. The amplitude of Ca²⁺ influx triggered by low-dose (100 nM) capsaicin was significantly higher in DRG neurons treated with PGE2 for 7 min than in untreated neurons (the majority of DRG neurons did not respond to low-dose capsaicin without prior sensitization; Fig. 5d,e), indicating that PGE2 treatment reduced TRPV1 activation thresholds. DRG neurons co-treated with PGE2 and TSP-1 for 7 min had a significant attenuation of the TRPV1 sensitization, compared to PGE2-only treated neurons, as indicated by reduced Ca²⁺ influx in response to low-dose capsaicin (Fig. 5d,e). To test whether TSP-1 also suppressed

sensitization of human sensory neurons, we generated human induced pluripotent stem (iPS) cell-derived sensory neurons³⁰ and used lentiviral transfection to express a fluorescent-based PKA activity sensor under a human Synapsin promoter to assess neuronal-specific PKA activity as indicated by GFP channel fluorescent intensity (Extended Data Fig. 8b). A significant induction of PKA activity immediately followed treatment with forskolin (FSK), an established PKA activator (Extended Data Fig. 8c,d). Pretreatment of iPS cell-derived sensory neuron culture with human TSP-1 for 10 min before FSK treatment decreased fluorescence of the PKA sensor in a dose-dependent manner (Extended Data Fig. 8c,d), suggesting a TSP-1-specific activity on neurons (Extended Data Fig. 8d). These findings validated predictions from the interactome model and highlighted a noncanonical role for TSP-1 in counteracting nociceptor sensitization.

Discussion

Here, we generated a comprehensive dataset of immune changes in the skin at the single-cell level as inflammatory pain hypersensitivity developed and resolved, which can serve as a resource to decipher cell subsets and immune mediators that govern specific types of acute inflammatory pain. In addition to revealing gene programs associated with pain development, we also found that pain resolution is not simply the absence of pain-inducing gene programs but includes the induction of novel immune gene signatures suggesting an active process. We highlighted representative genes significantly differentially expressed in individual immune cell types at T_{max} and T_{res} post-injury. The online portal <http://painseq.shinyapps.io/immune/> will enable further interrogation of immune gene programs responsive to various skin injuries.

The INDRA neuro-immune dataset was designed to be a general resource that contains as many potential interactions between immune cells and neurons as possible. These interactions were captured in a standardized intermediate format (INDRA statements), maintaining the provenance of the information⁶, which can be web-accessed. Several immune cell–nociceptor interactions predicted by the neuroimmune interactome at T_{max} , such as *Ptgs2–Ptgir*, *Aldh3a2–Mrgprd* and *Hbegf–Cd44* (refs. 2,23,31) are known to promote pain or itch by enhancing nociceptor activity, underscoring the predictive power of INDRA-based platform. The immune ligand TSP-1, in contrast, suppressed PGE2-induced nociceptor sensitization. In the central nervous system, TSP-1 is produced by astrocytes and promotes synaptogenesis³². TSP-1 also acts on endothelial cells to suppress vascularization and nitric oxide production and promotes platelet aggregation^{24,26}. We now report a role for TSP-1 in the peripheral nervous system. While the endogenous opioid system inhibits pain via actions on peripheral and central neurons that express the mu-opioid receptor (MOR) largely by reducing synaptic transmission³³, TSP-1 reduces the sensitization of the peripheral terminals of sensory neurons. Because neutrophils, *Ccr2*⁺ and *Ccr2*⁻ recMacs that produced TSP-1 also secrete pro-nociceptive inflammatory mediators such as PGE2, IL-1 β and TNF, TSP-1 is likely to fine-tune pain thresholds by the combined presence of both enhancers and suppressors of nociceptor sensitization in the complex immune milieu that develops in skin inflammation. This unbiased receptor–ligand interactome-based approach provided, therefore, a means for the comprehensive interrogation of exactly how the immune microenvironment encodes injury-specific and temporally regulated cues that are received by nociceptors to either heighten or reduce inflammatory pain sensitivity.

Online content

Any methods, additional references, Nature Portfolio reporting summaries, source data, extended data, supplementary information, acknowledgements, peer review information; details of author contributions and competing interests; and statements of data and code availability are available at <https://doi.org/10.1038/s41590-024-01857-2>.

References

- Basbaum, A. I., Bautista, D. M., Scherrer, G. & Julius, D. Cellular and molecular mechanisms of pain. *Cell* <https://doi.org/10.1016/j.cell.2009.09.028> (2009).
- Ricciotti, E. & Fitzgerald, G. A. Prostaglandins and inflammation. *Arterioscler. Thromb. Vasc. Biol.* **31**, 986–1000 (2011).
- Jain, A. & Pasare, C. Innate control of adaptive immunity: beyond the three-signal paradigm. *J. Immunol.* **198**, 3791–3800 (2017).
- Renthal, W. et al. Transcriptional reprogramming of distinct peripheral sensory neuron subtypes after axonal injury. *Neuron* **108**, 128–144.e9 (2020).
- Jain, A., Hakim, S. & Woolf, C. J. Unraveling the plastic peripheral neuroimmune interactome. *J. Immunol.* **204**, 257–263 (2020).
- Gyori, B. M. et al. From word models to executable models of signaling networks using automated assembly. *Mol. Syst. Biol.* **13**, 954 (2017).
- Kolter, J. et al. A subset of skin macrophages contributes to the surveillance and regeneration of local nerves. *Immunity* **50**, 1482–1497.e7 (2019).
- Kupari, J. & Ernfors, P. Molecular taxonomy of nociceptors and pruriceptors. *Pain* **164**, 1245–1257 (2023).
- Delfini, M. C. et al. TFAFA4, a chemokine-like protein, modulates injury-induced mechanical and chemical pain hypersensitivity in mice. *Cell Rep.* **5**, 378–388 (2013).
- François, A. et al. The low-threshold calcium channel Cav3.2 determines low-threshold mechanoreceptor function. *Cell Rep.* **10**, 370–382 (2015).
- Lukacs, N. W. et al. Stem cell factor (c-kit ligand) influences eosinophil recruitment and histamine levels in allergic airway inflammation. *J. Immunol.* **156**, 3945–3951 (1996).
- Talbot, S. et al. Silencing nociceptor neurons reduces allergic airway inflammation. *Neuron* **87**, 341–354 (2015).
- Serhan, N. et al. House dust mites activate nociceptor–mast cell clusters to drive type 2 skin inflammation. *Nat. Immunol.* **20**, 1435–1443 (2019).
- Tseng, P. Y. & Hoon, M. A. Oncostatin M can sensitize sensory neurons in inflammatory pruritus. *Sci. Transl. Med.* **13**, eabe3037 (2021).
- Ley, K. & Morris, M. Signals for lymphocyte egress. *Nat. Immunol.* <https://doi.org/10.1038/ni1205-1215> (2005)
- Bachman, J. A., Gyori, B. M. & Sorger, P. K. Automated assembly of molecular mechanisms at scale from text mining and curated databases. *Mol. Syst. Biol.* **19**, e11325 (2023).
- Efremova, M., Vento-Tormo, M., Teichmann, S. A. & Vento-Tormo, R. CellPhoneDB: inferring cell–cell communication from combined expression of multi-subunit ligand–receptor complexes. *Nat. Protoc.* **15**, 1484–1506 (2020).
- Türei, D. et al. Integrated intra- and intercellular signaling knowledge for multicellular omics analysis. *Mol. Syst. Biol.* **17**, e9923 (2021).
- Türei, D., Korcsmáros, T. & Saez-Rodriguez, J. OmniPath: guidelines and gateway for literature-curated signaling pathway resources. *Nat. Methods* <https://doi.org/10.1038/nmeth.4077> (2016).
- Bairoch, A. The ENZYME database in 2000. *Nucleic Acids Res.* <https://doi.org/10.1093/nar/28.1.304> (2000).
- Rodchenkov, I. et al. Pathway Commons 2019 Update: integration, analysis and exploration of pathway data. *Nucleic Acids Res.* **48**, 489 (2020).
- Jin, S. et al. Inference and analysis of cell–cell communication using CellChat. *Nat. Commun.* **12**, 1088 (2021).
- Liu, Q. et al. Mechanisms of itch evoked by β -alanine. *J. Neurosci.* **32**, 14532–14537 (2012).
- Isenberg, J. S. et al. Thrombospondin-1 stimulates platelet aggregation by blocking the antithrombotic activity of nitric oxide/cGMP signaling. *Blood* **111**, 613–623 (2008).

25. Isenberg, J. S. et al. CD47 is necessary for inhibition of nitric oxide-stimulated vascular cell responses by thrombospondin-1. *J. Biol. Chem.* **281**, 26069–26080 (2006).
26. Adams, J. C. & Lawler, J. The thrombospondins. *Cold Spring Harb. Perspect. Biol.* **3**, a009712 (2011).
27. Bhawe, G. et al. cAMP-dependent protein kinase regulates desensitization of the capsaicin receptor (VR1) by direct phosphorylation. *Neuron* **35**, 721–731 (2002).
28. Taiwo, Y. O., Heller, P. H. & Levine, J. D. Mediation of serotonin hyperalgesia by the cAMP second messenger system. *Neuroscience* **48**, 479–483 (1992).
29. Aley, K. O. & Levine, J. D. Role of protein kinase A in the maintenance of inflammatory pain. *J. Neurosci.* **19**, 2181–2186 (1999).
30. Deng, T. et al. Scalable generation of sensory neurons from human pluripotent stem cells. *Stem Cell Rep.* **18**, 1030–1047 (2023).
31. Wangzhou, A. et al. A ligand–receptor interactome platform for discovery of pain mechanisms and therapeutic targets. *Sci. Signal* **14**, eabe1648 (2021).
32. Christopherson, K. S. et al. Thrombospondins are astrocyte-secreted proteins that promote CNS synaptogenesis. *Cell* **120**, 421–433 (2005).
33. Ruiz-Cantero, M. C. et al. The sigma-1 receptor curtails endogenous opioid analgesia during sensitization of TRPV1 nociceptors. *Br. J. Pharmacol.* **180**, 1148–1167 (2023).

Publisher's note Springer Nature remains neutral with regard to jurisdictional claims in published maps and institutional affiliations.

Open Access This article is licensed under a Creative Commons Attribution 4.0 International License, which permits use, sharing, adaptation, distribution and reproduction in any medium or format, as long as you give appropriate credit to the original author(s) and the source, provide a link to the Creative Commons licence, and indicate if changes were made. The images or other third party material in this article are included in the article's Creative Commons licence, unless indicated otherwise in a credit line to the material. If material is not included in the article's Creative Commons licence and your intended use is not permitted by statutory regulation or exceeds the permitted use, you will need to obtain permission directly from the copyright holder. To view a copy of this licence, visit <http://creativecommons.org/licenses/by/4.0/>.

© The Author(s) 2024

¹F. M. Kirby Neurobiology Center, Boston Children's Hospital, Boston, MA, USA. ²Laboratory of Systems Pharmacology, Harvard Medical School, Boston, MA, USA. ³Khoury College of Computer Sciences, Northeastern University, Boston, MA, USA. ⁴Department of Bioengineering, College of Engineering, Northeastern University, Boston, MA, USA. ⁵Department of Neurobiology, Harvard Medical School, Boston, MA, USA. ⁶Research Computing, Department of Information Technology, Boston Children's Hospital, Boston, MA, USA. ⁷Department of Neurology, Brigham and Women's Hospital and Harvard Medical School, Boston, MA, USA. ⁸Program in Neurogenetics, Department of Neurology, David Geffen School of Medicine, University of California Los Angeles, Los Angeles, CA, USA. ⁹Center for Neurobehavioral Genetics, Semel Institute for Neuroscience and Human Behavior, University of California Los Angeles, Los Angeles, CA, USA. ¹⁰Department of Pharmacology and Neurosciences Institute (Biomedical Research Center) and Biosanitary Research Institute ibs.GRANADA, University of Granada, Granada, Spain. ¹¹Salk Institute for Biological Studies, La Jolla, CA, USA. ¹²Department of Anesthesiology, Faculty of Medicine, University of Yamanashi, Chuo, Yamanashi, Japan. ¹³Department of Systems Biology, Harvard Medical School, Boston, MA, USA. ✉ e-mail: clifford.woolf@childrens.harvard.edu

Methods

Mice

Eight-to-12-week-old C57BL/6J mice were obtained from the Jackson Laboratory (JAX:000664) as were Cd47-deficient mice (Jax:003173)³⁴. Both male and female mice were used in all the behavior experiments. scRNA-seq was performed on female mice. No statistical methods were used to predetermine sample sizes, but our sample sizes are similar to those reported in previous publications^{35,36}. All animal experiments were conducted according to institutional animal care and safety guidelines at Boston Children's Hospital and Harvard Medical School.

Inflammatory pain models

For each model, mice were randomly selected from the cage to receive the inflammatory stimulus. All mice in a cage received the same inflammatory stimulus, and the person inducing the inflammation was different from the person testing for hypersensitivity who was fully blinded.

Paw skin incision. The mice were anesthetized by administration of 2.5% isoflurane. A 3–5 mm skin incision was made using a surgical sterile scalpel on the plantar surface of the mouse paw without cutting through the underneath muscle. The skin was sutured using 6–0 silk surgical suture (Ethicon, K889H) in an aseptic manner. The CL control was left untouched.

UV burn. Mice were anesthetized by administration of 2.5% isoflurane. Mouse hind paws were exposed to UV irradiation at an intensity of 1 J cm⁻² for 2 min using a wavelength 305–315 nm fluorescent UV-B light source. The CL control was not exposed to UV.

Zymosan. The mice were anesthetized by administration of 2.5% isoflurane. Twenty microliters of 5 mg ml⁻¹ zymosan (in saline) was injected into the plantar surface of the hind paw. Saline was injected into the CL control.

Hargreaves thermal testing

The mice were habituated to the Hargreaves's apparatus (IITC #390G) consisting of a glass floor heated to 30 °C and a plexiglass chamber for 2 days before testing, 1 h per day. On the day of assessment, the mice were habituated for another 1 h before the test. A focused radiant heat light (15% intensity) source was focused on the plantar surface of the left paw of mice, and a ramping heat stimulus was applied until a paw withdrawal was recorded. Readings were averaged from two trials. Blinded testing of mice with paw incision and zymosan injection was not possible since it was clear to see which paw was inflamed, but the operator was not told which foot the UV burn had been applied to, thus aiding blinding for those mice.

Tissue processing of mouse plantar skin

The planter skin of the mouse hind paw was dissected, separating the muscle and collected into 1% bovine serum albumin (BSA) containing RPMI. The skin was minced using scissors into 1–2 mm pieces. Liberase TM (Roche) was added to the medium at a final concentration of 0.5 mg ml⁻¹. Tissue was digested at 37 °C while vortexing at 400g for 90 min. The digested tissue was strained using a 100 µm strainer to obtain a single-cell suspension used for flow sorting on BD ARIAll and single-cell transcriptomics.

Flow cytometry

Cells were washed with FACS buffer and incubated with Fc block for 10 min on ice. Cells were then stained with mouse antibodies against mouse flow cytometry antibodies include CD45-FITC (1:400, BioLegend, cat. no. 103107), CD64-PE-594 (1:600, BioLegend, cat. no. 139319), CD11c-APC (1:400, BioLegend, cat. no. 101211) Cd11b-eFluor 780 (1:400, eBioscience, cat. no. 47-0112-82), Ly6G-PE (1:800, BioLegend, cat. no. 127607) and Ly6c-BV711 (1:2,000, BioLegend, cat. no.

128037) for 30 min on ice. Cells were washed and then resuspended with 3 µM 4',6-diamidino-2-phenylindole (DAPI) for analysis. All flow cytometry analysis was performed on BD Fortessa. All data analysis was performed on FlowJo 10.

scRNA-seq of immune cells (10x Genomics)

For isolation of immune cells for single-cell sequencing, cells were washed with FACS buffer and incubated with Fc block for 10 min on ice. Cells were then stained with anti-mouse CD45-FITC antibody for 30 min at 4 °C. CD45⁺ DAPI-negative cells were sorted to a 90% purity using BD ARIAll at Boston Children's Hospital Flow cytometry core. Cells were collected into 0.5% BSA containing phosphate-buffered saline (PBS) without EDTA. Single-cell suspensions were encapsulated into droplets using the Chromium Next GEM Single Cell 3' Reagent kit v3.1 (Dual Index).

scRNA-seq library preparation

scRNA-seq libraries were prepared using Chromium Next GEM Single Cell 3' Reagent Kit v3.1 (10x Genomics), following the manufacturer's protocols. Briefly, to generate single-cell gel-bead-in-emulsion (GEM) solution, sorted cells were resuspended in a final volume of 40 µl and were loaded on a Next GEM Chip G (10x Genomics) and processed with the 10x Genomics Chromium Controller. Reverse transcription was performed as instructed: 53 °C for 45 min and 85 °C for 5 min in a thermocycler. Next, first-strand complementary DNA was cleaned with DynaBeads MyOne SILANE (10x Genomics, 2000048) and then amplified, followed by cleanup with SPRIselect Reagent kit (Beckman Coulter, B23318). The cDNAs were examined on High-Sensitivity DNA Chip with Bioanalyzer (Agilent). Ten microliters of cDNA was forwarded to the library preparation. The dual-indexed libraries were examined on High-Sensitivity DNA Tape with TapeStation (Agilent) before being pooled for sequencing. The sequencing was performed with a NovaSeq 6000 (Illumina) at an estimated depth of 65,000–233,000 reads per cell. The raw scRNA-seq data were preprocessed using Cell Ranger v7.1.0 (10x Genomics), including aligning reads to the mouse reference genome (mm10-2020-A) and generating expression count matrices. The count matrices were further processed as described below.

Initial quality control, clustering and visualization of scRNA-seq

Using the generated expression count matrices, an in-house scRNA-seq pipeline was built on the basis of the Seurat R package (R v4.2.3, Seurat v4.3.0)^{37,38}, including quality control, cell filtering, spectral clustering, cell type annotation, differential gene expression and visualization. Multiplets were identified using the scds package (v1.14.0) using the `cxds` function³⁹. Only identified singlets were kept for further analysis. We filtered out cells exhibiting extremely low or high library sizes and number of gene features, falling outside the 95% confidence interval, as well as those displaying high mitochondrial content (above the 5%). The cell counts pre- and post-filtering in each sample are included in Supplementary Table 1. Cells of good quality from the two replicates per group were merged, and the 12 experimental groups were integrated for analysis using Harmony⁴⁰. Principal component analysis over the identified 2,000 highly variable genes was applied for data dimension reduction (dimensions 60) before cell clustering. Cell clustering was performed on integrated data with a shared nearest-neighbor graph-based method using the `FindNeighbors` function included in Seurat, followed by the Louvain algorithm for modularity optimization (resolution 2) using `FindClusters` function. After the cell clusters were determined, their top marker genes were identified with the `FindAllMarkers` function. For cluster annotation, the top marker genes based on the adjusted *P* value were manually curated to match canonical cell types and their marker genes based on literature research and public resources from scRNA-seq databases. The curated annotations are further supported by the automatic annotations using the SingleR tool

(v2.0.0)⁴¹. For differentially expressed genes, the default parameters of the FindMarkers function from Seurat were used which is the Wilcoxon rank-sum test with \log_2 fold change (FC) threshold of 0.25 and min.pct of 0.1 with adjusted *P* value < 0.05.

scCODA analysis

The cell-type compositional data analysis across the different injuries and time points using the scRNA-seq was carried out by using scCODA (v0.1.9)⁴². It uses a Bayesian approach along with a spike and slab before determining the credible effects on the basis of the inclusion probability. We used a false discovery rate cutoff of 0.05 to determine the significant proportion differences between the different groups on the basis of the credible effects.

DiVenn plots

DiVenn tool (<https://divenn.tch.harvard.edu/v2/>) was used to compare the differentially expressed genes between different time points for selected cell types⁴³. It visualizes the unique and common genes between time point comparisons in the form of networks. The upregulated and downregulated genes are marked as red and blue, respectively. The genes that are upregulated in one comparison and downregulated in others (or vice versa) are marked as yellow.

Analysis of DRG neuron snRNA-seq data

DRG neuron snRNA-seq data were obtained from previously published data⁴. Neuronal cells from naive mice (male and female) were obtained by subsetting the Seurat object based on annotation. The neuron data are merged with the immune scRNA-seq data and are then scaled and normalized to be further used for the cell–cell communication analysis. For differential gene expression, the FindAllMarker function employing test.use = 'wilcox', Wilcoxon rank-sum test was used. A threshold of \log_2 FC 0.8 and min.pct 0.25 and adjusted *P* < 0.05 was applied.

Assembling the cell–cell interactome

INDRA 1.21.0 was used to assemble the interactome. The list of receptors was obtained from CellPhoneDB 2.1.7, using the protein_generated.csv file generated by CellPhoneDB's generate_proteins function. OmniPath interactions were obtained on 22 March 2022, through INDRA's OmniPath API, which uses the <http://omnipathdb.org/interactions> endpoint of the OmniPath web service to obtain the 'ligreextra' subset of interactions corresponding to ligand–receptor interactions. These interactions were then filtered for curation effort > 0, to ones containing human proteins only, and to the following OmniPath source identifiers corresponding to sources of cell–cell interaction information: 'CellPhoneDB', 'Guide2Pharma', 'HPMR', 'ICELNET', 'Kiroac2010', 'CellTalkDB', 'CellChatDB', 'connectomeDB2020', 'Ramilowski2015' and 'talklr'. The ligand list was derived by taking the 'source' participant of OmniPath interactions with a well-defined consensus direction and excluding known receptors. The ion channel list was derived from a curated list of proteins from the Illuminating the Druggable Genome project at <https://druggablegenome.net/>, removing overlaps with any receptors and ligands. The enzyme list was obtained from ExPasy at <ftp://ftp.expasy.org/databases/enzyme/enzyme.dat> via PyOBO (<https://github.com/pyobo/pyobo>) to extract proteins that belong to any enzyme class, then filtered out any proteins known to be kinases or phosphatases on the basis of lists maintained by INDRA. Ligand–receptor interactions were taken from the overall OmniPath interaction list by filtering to interactions containing one ligand and one receptor. Evidence from publications and further structured databases aligned with these interactions was then obtained via INDRA. Ligand–ion channel interactions were obtained from INDRA directly by filtering Complex and Activation INDRA Statement types and Statements containing one ligand and one ion channel per the gene lists above. Statements were also filtered to ones supported by structured databases or at least two supporting sentences from text mining. Interactions involving

enzymes were obtained in two parts. First, Pathway Commons v12 data were obtained in SIF format from <https://www.pathwaycommons.org/archives/PC2/v12/PathwayCommons12.Detailed.hgnc.sif.gz> and filtered to controls-production-of-interaction whose controller is in the list of enzymes. The set of products for each enzyme was determined from the collection of rows remaining after these filters. For each enzyme product, INDRA was then used to find Activation and Complex Statements in which the enzyme product interacts with a receptor or an ion channel. Finally, enzyme–receptor and enzyme–ion channel interactions were generated by connecting an enzyme to a receptor or ion channel if its product interacts with the given receptor or ion channel. Finally, the interactome was exported into a tabular format compatible with CellChat using UniProt IDs to identify interacting proteins.

Identification of significant interactions for cell–cell pairs

We used CellChat (v1.6.1) along with the assembled database of ligands and receptor pairs for mice to identify patterns of cell-to-cell communication²². To assess the likelihood of communication, we followed the methodologies outlined in the original research paper by Jin et al.²². We applied these methods at the ligand–receptor pair level. To ensure reliable and significant findings, communication between cell types observed in fewer than ten cells with adjusted *P* values greater than 0.05 were excluded. The plots were generated using the built-in functions within CellChat.

Isolation and in vitro culture of DRG neurons

Lumbar and thoracic DRG were obtained from mice and collected in Dulbecco's modified Eagle medium containing fetal calf serum and penicillin and streptomycin (DMEM). DRG were digested in Collagenase A (Roche, 5 mg ml⁻¹) and Dispase II (Roche, 1 mg ml⁻¹) for 70 min. Digested DRG were triturated using large-, medium- and small-sized polished glass pipettes in DMEM containing DNase. The cells were resuspended in DMEM and overlaid on 10% BSA solution. The bilayer was centrifuged for 12 min at 1,000g at reduced acceleration and deceleration. The top two layers were discarded, and the cell pellet was collected. For Ca imaging, cells were cultured at the center of a PDL (500 µg ml⁻¹) and Laminin (5 mg ml⁻¹) coated 35 mm dish in Neurobasal A Media (Life Technologies, 10888-022) containing 2% B-27, penicillin, streptomycin, 10 µM arabinocytidine (Sigma) and GDNF (5 ng ml⁻¹, Sigma-Aldrich, SRP3200). A total of 5,000–8,000 cells were plated in a 50–80 µl drop and replenished with 2 ml of medium per dish and incubated at 37 °C and 5% CO₂ for 48 h before calcium imaging experiments.

Calcium imaging of DRG neurons

After 48 h in culture, DRG neurons were loaded with 4 µg ml⁻¹ of Fura2-AM (Invitrogen) by incubating for 50 min at room temperature (RT). Cells were then washed with standard extracellular solution (SES) twice and left in 2 ml of SES to be used as recording solution. Live imaging was performed on Nikon Eclipse Ti microscope (Nikon) with standard 340- and 380-nm filters controlled by a Ludl Mac6000 shutter using Nikon Elements software. Frames were recorded every 3 s. All imaging was performed at RT. Cell treatments were performed using a gravity-based perfusion system. Cells were simply treated with SES for 2 min to get stable images and remove perfusion related artifacts. Then, cells were exposed to with freshly prepared PGE2 (1 µM) ± TSP-1 (200 ng ml⁻¹) for 7 min, followed by the application of a low concentration of capsaicin (0.1 µM) for 30 s with or without PGE2 or TSP-1. After a 5 min perfusion of SES, a high concentration of capsaicin (1 µM) was applied at RT for 30 s, to identify all capsaicin-sensitive TRPV1⁺ neurons.

Immunohistochemistry

DRG were collected in PBS and then fixed in 4% paraformaldehyde on a shaker at 4 °C for 30 min. After fixation, DRG were moved to 30% sucrose overnight, then mounted in OCT and frozen. DRG were sectioned at 20 µm, mounted onto SuperFrost Plus microscope slides and

stored at -20°C . Slides were thawed for 30 min, then washed with PBS for 15 min. Slides were incubated in blocking buffer for 2 h at RT (10% donkey serum, 0.4% Triton-X, 0.05% Tween 20 and 1% BSA) and then incubated in primary antibody overnight at 4°C (Rb anti-PGP9.5 abcam ab108986 1:500, goat anti-CD47 RnD Systems AF1866 1:200). Slides are then washed $3\times$ in PBS and incubated in secondary antibody at RT for 2 h (donkey anti-Rb Cy3 Jackson ImmunoResearch 711-165-152 1:500, donkey anti-goat 647 Thermo Fisher A-21447 1:500). Slides were finally washed $3\times$ with PBS and mounted with Prolong anti-fade DAPI medium. Stained slides were imaged on a Leica SP8 confocal microscope with a $63\times$ oil objective. Z-stacks spanning the tissue were taken, and four adjacent fields were tiled. ImageJ was used to obtain the maximum intensity projection.

Molecular cloning

The ExRai-AKAR2 PKA reporter was cloned into a lentiviral backbone under the human synapsin promoter from a previously reported construct^{44,45}. The lentiviral vector used to overexpress the PKA sensor in our study, pLV[Exp]-SYN1>PKAsub/ExRai2:WPRE, was constructed and packaged by Vector Builder. The vector ID is VB220620-1230gm, which can be used to retrieve detailed information about the vector on vectorbuilder.com.

Human iPSC cell-derived sensory neuron differentiation and viral transfection

This study was approved by the institutional review board at Boston Children's Hospital (IRB-P00006313). Human iPSC cells (Lonza, LiPS-GR1.1) were thawed and expanded in E8 medium (Thermo Fisher Scientific, cat. no. A1517001) for three passages before onset of differentiation. iPSC cells were passaged using the ReLeSR agent (Stem Cell Technologies, cat. no. 05872) and coated on vitronectin substrate (Thermo Fisher Scientific, A14700). iPSC cells were differentiated into sensory neurons following previously established protocols³⁰. In brief, iPSC cells were plated in six-well plates at a density of 1.5×10^6 cells per well and treated with $0.2 \mu\text{M}$ CHIR-98014 (SelleckChem, cat. no. S2745) and $2 \mu\text{M}$ A83-01 (Tocris, cat. no. 2939/10) in E6 medium (Thermo Fisher Scientific, cat. no. 1516401) for 3 days. Cells were then replated at 5.5×10^5 cells per well in six-well AggreWell plates (Stem Cell Technologies) and further differentiated for 11 days in E6 medium containing $0.5 \mu\text{M}$ CHIR-98014, $2 \mu\text{M}$ A83-01, $1 \mu\text{M}$ DBZ (Tocris, cat. no. 4489/10) and 25 nM PD173074 (Tocris, cat. no. 3044/10). On day 14 from the onset of differentiation, nocispheres were dissociated using the MACS EB dissociation kit (Miltenyi Biotec, cat. no. 130-096-348) into single cells. Cells are then frozen in Neuron Freezing Media (Cell Applications, 042-50) or plated at 5,000 neurons per well in 384-well plates in neuron maturation medium containing DMEM/F12 (Thermo Fisher Scientific, cat. no. 11320082), B27 Supplement (Thermo Fisher Scientific, cat. no. a3353501), N2 Supplement (Thermo Fisher Scientific, cat. no. A1370701) with 25 ng ml^{-1} BDNF (Thermo Fisher Scientific, cat. no. PHC7074), 25 ng ml^{-1} GDNF (Thermo Fisher Scientific, PHC7045), 25 ng ml^{-1} β -NGF (Thermo Fisher Scientific, PHG0126), 25 ng ml^{-1} NT-3 (Thermo Fisher Scientific, PHC7036) and CEPT cocktail⁴⁶. After 24 h, CEPT cocktail was removed and replaced with $1 \mu\text{M}$ PD0332991 (Tocris, cat. no. 4786/10). Half-medium changes were performed every 3 days for 14 further days of neuronal maturation. On day 7, after the onset of neuronal maturation, cells were transduced with a lentiviral vector at a multiplicity of infection of 5 for 24 h before complete medium change was performed.

Human iPSC cell sensory neuron treatment and imaging analysis

On day 14 of neuronal maturation, cells were treated with TSP-1 (RnD systems 3074-TH) at varying concentrations for 10 min. Cells were then imaged at $20\times$ magnification in FITC channel at 150 ms exposure using ImageXpress Micro Confocal (Molecular Devices) before the addition of $10 \mu\text{M}$ FSK (Tocris 1099) (pre-image). Cells were again imaged

immediately after the application of FSK (post-image). All images were subjected to background removal in Fiji ImageJ software. Cell bodies were identified, and their intensity in pre- and post-FSK treatment images was measured using Cell Profiler software⁴⁷. FC in total cell body intensity was calculated for each well.

Data and statistical analysis

Statistical analysis, including animal numbers (n) and P values, are included in the figure legends. Statistical analysis was performed using GraphPad Prism 9. Data distribution was assumed to be normal, but this was not formally tested. All single-cell sequencing analysis was performed using R version 4.2.3. The web resource used to present our data (<http://painseq.shinyapps.io/immune/>) was built using R shiny apps and Shiny Cell v2.1 (ref. 48).

Reporting summary

Further information on research design is available in the Nature Portfolio Reporting Summary linked to this article.

Data availability

Raw immune cell scRNA-seq files from healthy and injured skin samples will be deposited at the Gene Expression Omnibus repository (GEO) with a GEO accession number (GSE255686). The analyzed dataset from immune cell scRNA-seq is also available at <http://painseq.shinyapps.io/immune/>.

Code availability

Source code to generate the interactome and the interactome gene lists used in this study is available at https://github.com/gyorilab/neuroimmune_interactome.

References

- Lindberg, F. P. et al. Decreased resistance to bacterial infection and granulocyte defects in IAP-deficient mice. *Science* **274**, 795–798 (1996).
- Zhang, Z. et al. Automated preclinical detection of mechanical pain hypersensitivity and analgesia. *Pain* **163**, 2326–2336 (2022).
- Ghasemlou, N., Chiu, I. M., Julien, J. P. & Woolf, C. J. CD11b⁺ Ly6G⁺ myeloid cells mediate mechanical inflammatory pain hypersensitivity. *Proc. Natl Acad. Sci. USA* **112**, E6808–E6817 (2015).
- Stuart, T. et al. Comprehensive integration of single-cell data. *Cell* **177**, 1888–1902.e21 (2019).
- Butler, A., Hoffman, P., Smibert, P., Papalexi, E. & Satija, R. Integrating single-cell transcriptomic data across different conditions, technologies, and species. *Nat. Biotechnol.* **36**, 411–420 (2018).
- Bais, A. S. & Kostka, D. Scds: Computational annotation of doublets in single-cell RNA sequencing data. *Bioinformatics* **36**, 1150–1158 (2020).
- Korsunsky, I. et al. Fast, sensitive and accurate integration of single-cell data with Harmony. *Nat. Methods* **16**, 1289–1296 (2019).
- Aran, D. et al. Reference-based analysis of lung single-cell sequencing reveals a transitional profibrotic macrophage. *Nat. Immunol.* **20**, 163–172 (2019).
- Büttner, M., Ostner, J., Müller, C. L., Theis, F. J. & Schubert, B. scCODA is a Bayesian model for compositional single-cell data analysis. *Nat. Commun.* **12**, 6876 (2021).
- Sun, L. et al. Divenn: an interactive and integrated web-based visualization tool for comparing gene lists. *Front. Genet.* **10**, 421 (2019).
- Zhang, J. F. et al. An ultrasensitive biosensor for high-resolution kinase activity imaging in awake mice. *Nat. Chem. Biol.* **17**, 39–46 (2021).

45. Linghu, C. et al. Spatial multiplexing of fluorescent reporters for imaging signaling network dynamics. *Cell* **183**, 1682–1698.e24 (2020).
46. Tristan, C. A. et al. Efficient and safe single-cell cloning of human pluripotent stem cells using the CEPT cocktail. *Nat. Protoc.* **18**, 58–80 (2023).
47. Stirling, D. R. et al. CellProfiler 4: improvements in speed, utility and usability. *BMC Bioinform.* **22**, 433 (2021).
48. Ouyang, J. F., Kamaraj, U. S., Cao, E. Y. & Rackham, O. J. L. ShinyCell: simple and sharable visualization of single-cell gene expression data. *Bioinformatics* **37**, 3374–3376 (2021).

Acknowledgements

We thank the Research Computing Bioinformatics at BCH and the HMS Single Cell Core at HMS for their services and advice on experimental strategy and analysis. This study was funded by a DARPA PANACEA grant HR0011-19-2-0022 to C.J.W. and P.K.S., a DARPA Young Faculty Award W911NF-20-1-0255 to B.M.G., an NIH R35NS105076 to C.J.W., a Jane Coffin Childs Fund to Aa.J. and the Dr. Miriam and Sheldon G. Adelson Medical Research Foundation (C.J.W. and R.K.). We also thank E. Boyden at the Massachusetts Institute of Technology for sharing the ExRaiAKAR2 plasmid. The funders had no role in study design, data collection, and analysis, the decision to publish or preparation of the manuscript.

Author contributions

Aa.J. conceptualized the study, performed experiments, analyzed the data and wrote the manuscript. B.M.G. conceptualized and compiled the INDRA-based interactome and edited the manuscript. S.H., V.P., S.Z., D.G.T., M.C.R.-C., C.T.-L., N.A. and M.K. performed experiments.

As.J., L.S., S.A.B., Q.W., R.K. and S.B. performed bioinformatics analysis. W.R. and P.K.S. supervised the study. C.J.W. supervised the study and edited the manuscript.

Competing interests

C.J.W. is a founder of Nocion Therapeutics, Quralis and Blackbox Bio, an SAB member of Lundbeck, Axonis and Tafalgie Therapeutics, and a consultant for GSK. P.K.S. is a member of the Board of Directors of Glencoe Software and Applied Biomath, a member of the SAB for RareCyte, NanoString and Montai Health, and a consultant for Merck. The remaining authors declare no competing interests.

Additional information

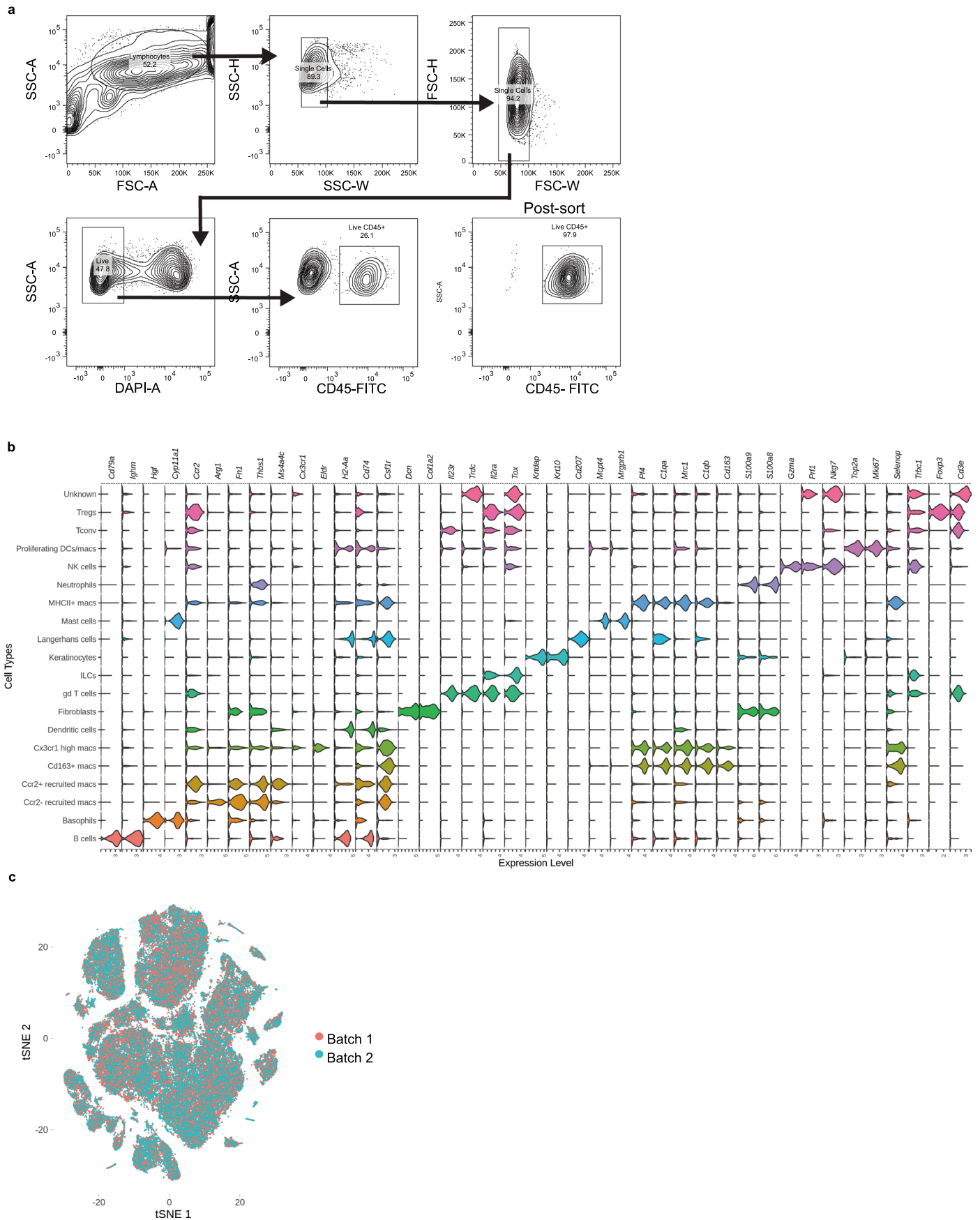
Extended data is available for this paper at <https://doi.org/10.1038/s41590-024-01857-2>.

Supplementary information The online version contains supplementary material available at <https://doi.org/10.1038/s41590-024-01857-2>.

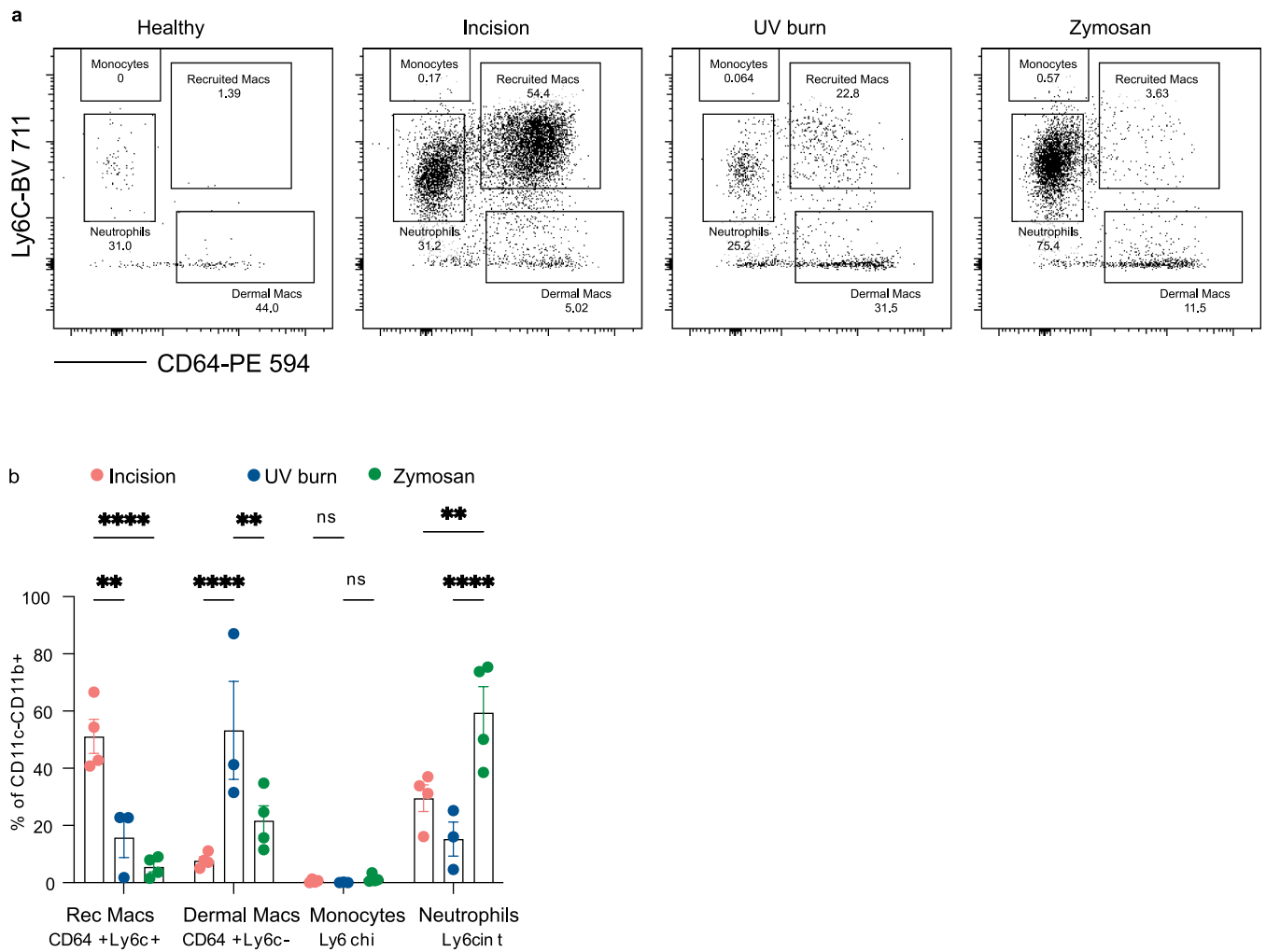
Correspondence and requests for materials should be addressed to Clifford J. Woolf.

Peer review information *Nature Immunology* thanks Daniel Mucida and the other, anonymous, reviewer(s) for their contribution to the peer review of this work. Ioana Staicu was the primary editor on this article and managed its editorial process and peer review in collaboration with the rest of the editorial team.

Reprints and permissions information is available at www.nature.com/reprints.

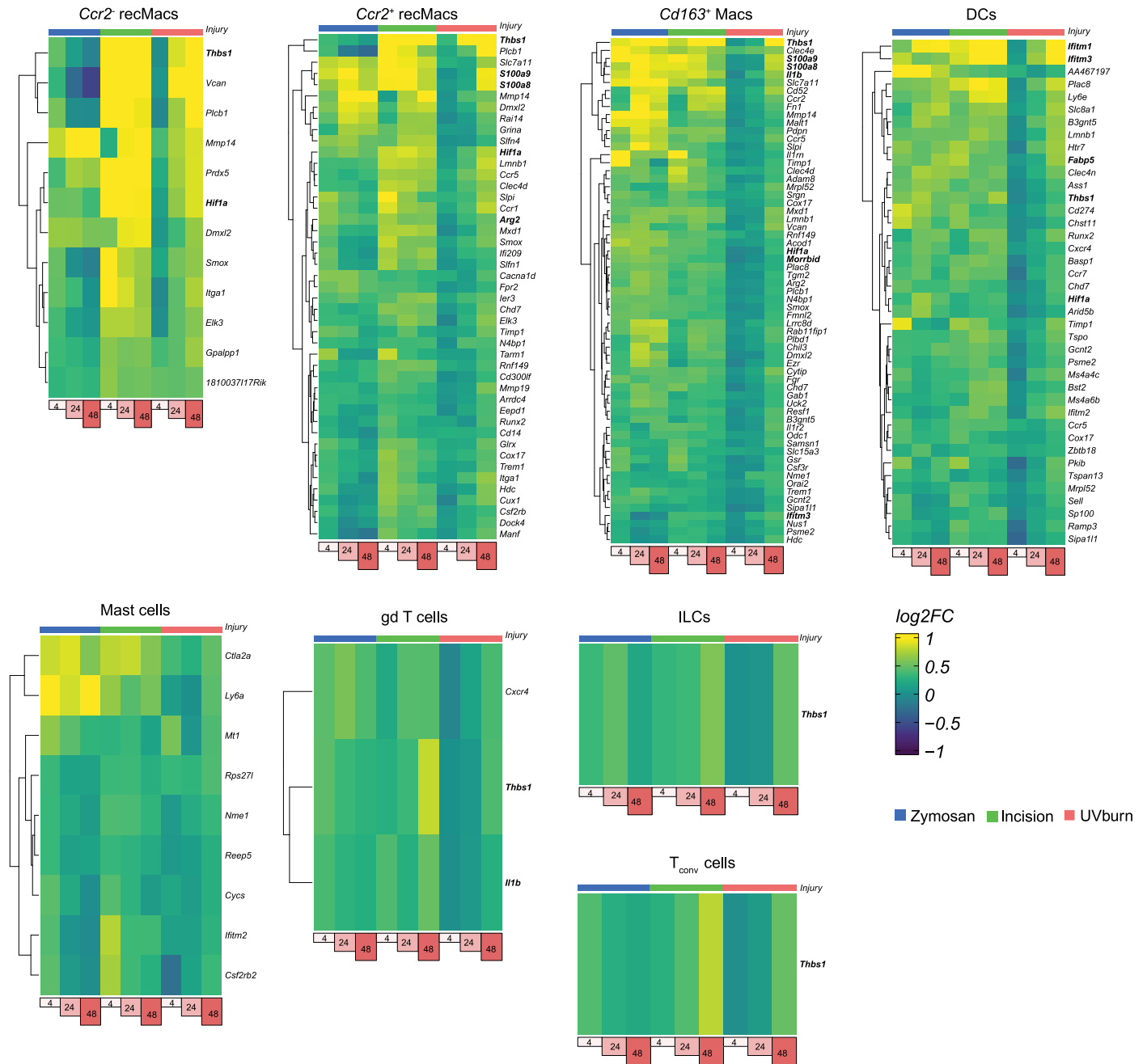


Extended Data Fig. 1 | Single-cell RNA sequencing analysis of immune cells. (a) Gating strategy for CD45+ cells from digested skin single cell suspension. **(b)** Violin plot marker genes used to cell type annotation **(c)** t-SNE plot showing the overlap between the two biological replicates.



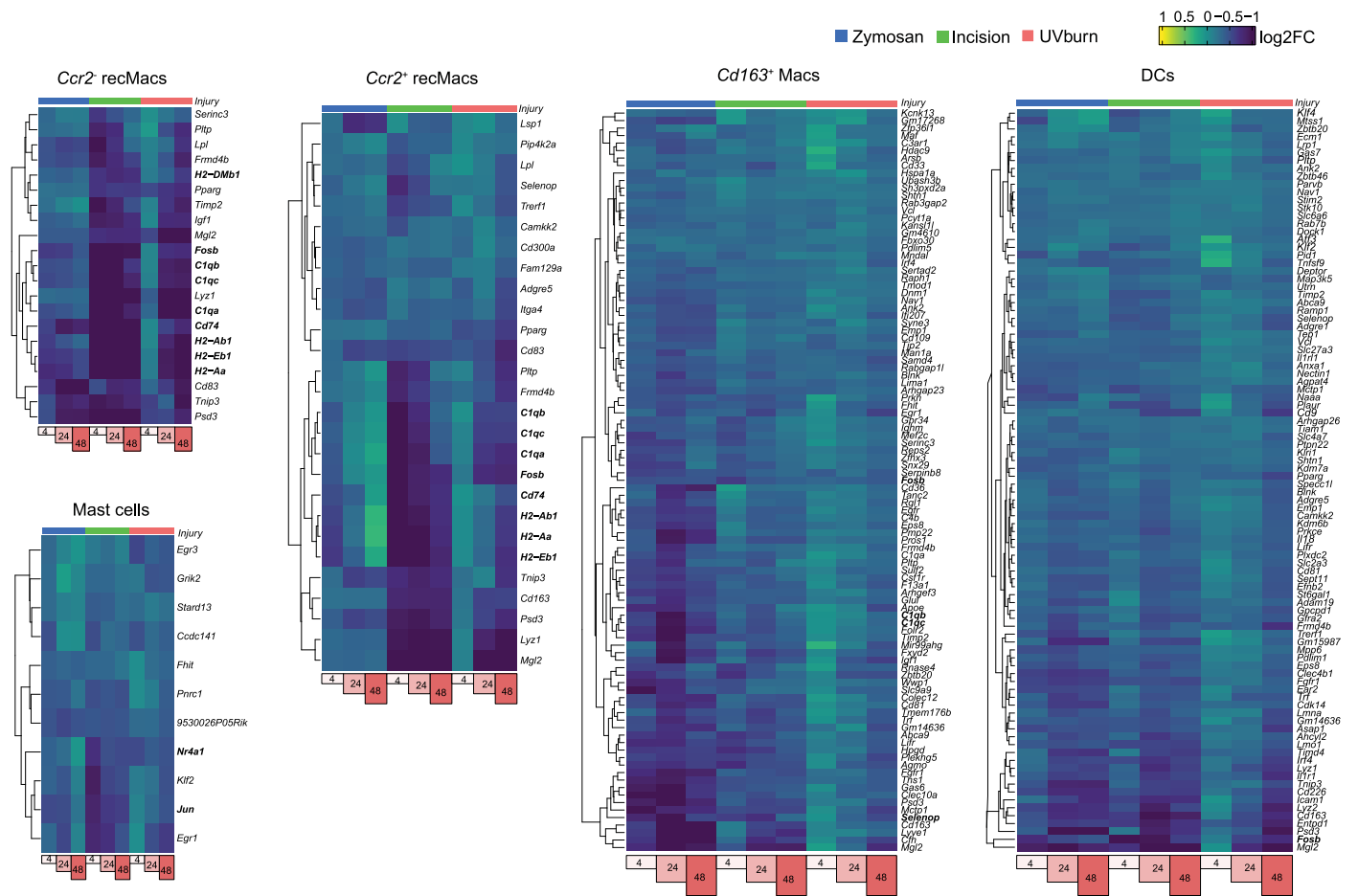
Extended Data Fig. 2 | Different injuries show distinct myeloid cell populations at T_{max}. Immune cells were isolated from injured or healthy paw skin and stained for various myeloid cell markers. **(a)** Immune cells isolated from injured paw skin stained for myeloid cell markers. Representative flow plots are gated on Live CD45 + CD11b + CD11c-cells. **(b)** Quantification of myeloid cell

populations in incision (24 h) (n = 4), UV burn (48 h) (n = 3), and zymosan (4 h) (n = 4). Data is gated on live CD45 + CD11b + CD11c- cells. Data are represented as mean value ± SEM. p values calculated using one-way ANOVA, Tukey's multiple comparison test. * p < 0.05, ** p, 0.01, *** p < 0.001, **** p < 0.0001, ***** < 0.00001 and n.s. = not significant.



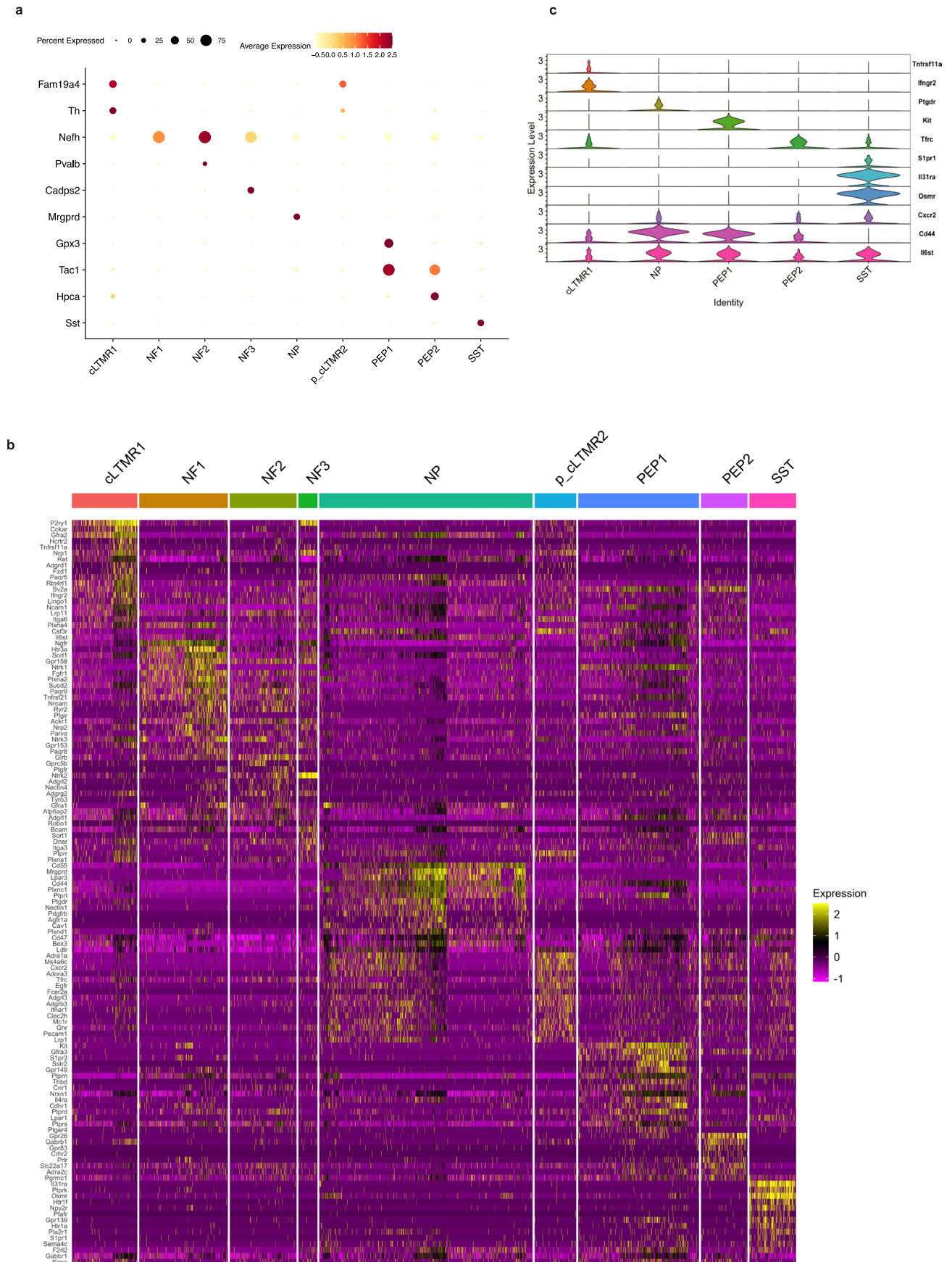
Extended Data Fig. 3 | Immune cells in zymosan, incision and UV burn show commonly upregulated genes at T_{max} . Heatmaps showing the log₂ fold-change of the commonly upregulated differentially expressed genes common in

zymosan, incision, and UV burn at T_{max} compared to CL_{zymosan}, CL_{incision} and CL_{UVB} respectively in *Ccr2* recMacs, *Ccr2*⁺ recMacs, *Cd163*⁺ Macs, dendritic cells, mast cells, gd T cells, ILCs and T_{conv} cells.



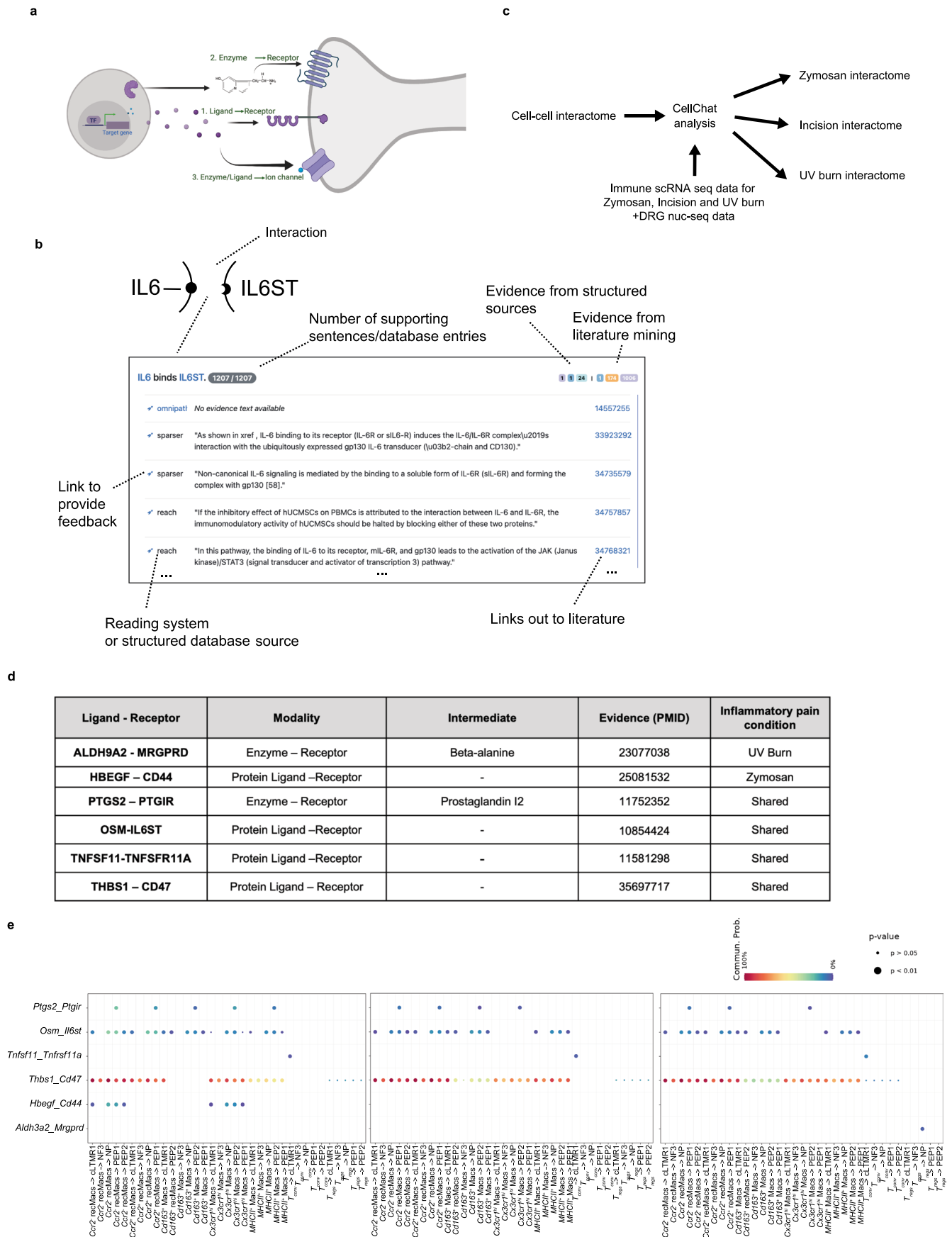
Extended Data Fig. 4 | Immune cells in zymosan, incision and UV burn show commonly downregulated genes at T_{max} . Heatmaps showing the log₂ fold-change of the commonly downregulated differentially expressed genes common

in zymosan, incision, and UV burn at T_{max} compared to CL_zymosan, CL_incision and CL_UVB respectively in *Ccr2* recMacs, *Ccr2*⁺ recMacs, *Cd163*⁺ Macs, dendritic cells and mast cells.



Extended Data Fig. 5 | Receptor expression profile in male DRG neurons. (a) Dot plot showing marker genes used to annotate given DRG subtypes. **(b)** Differential expression of receptor genes in cLTMR1, NF1, NF2, NF3, NP, p_cLTMR2, PEP1, PEP2 and SST, and cLTMR cells from male DRG neurons, from ref. 4. Heatmaps show

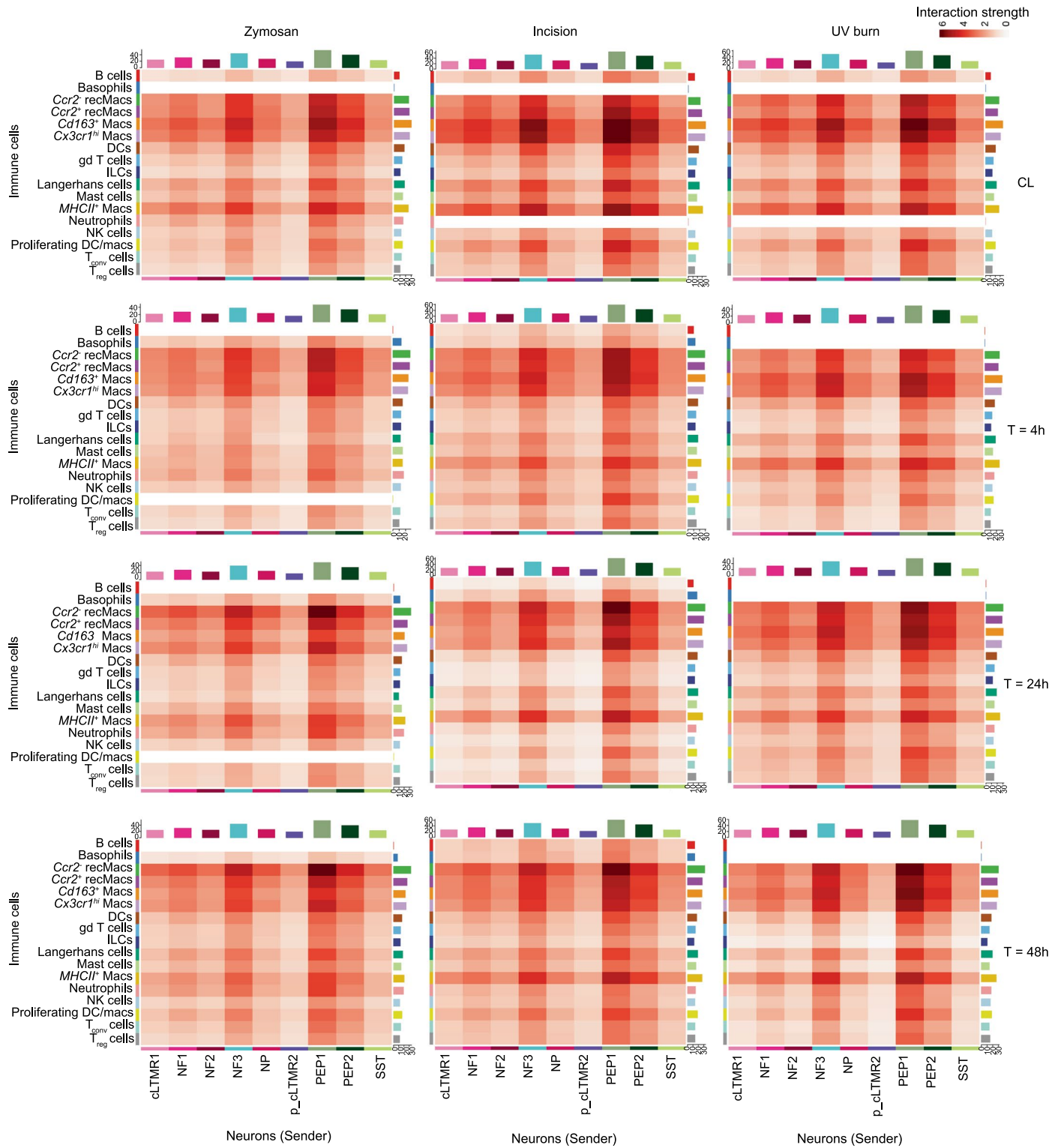
significantly (adjusted $p < 0.05$) differentially expressed genes in neurons with $\log_2FC = 0.5$ and min. pct. = 0.25. **(c)** Violin plot showing normalized expression of specific receptor genes in cLTMR1, PEP1, PEP2, NP and SST neurons.



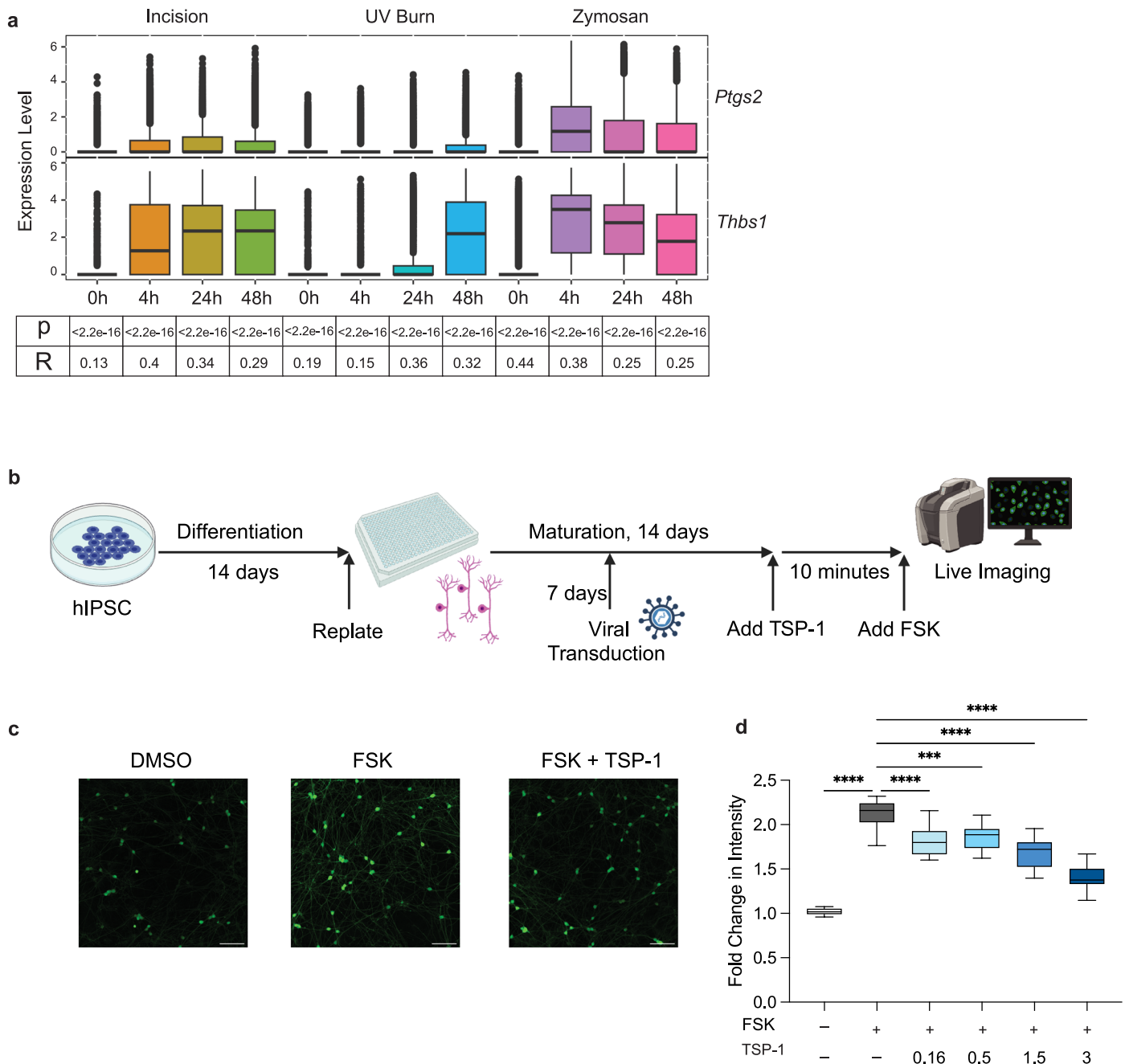
Extended Data Fig. 6 | See next page for caption.

Extended Data Fig. 6 | Neuroimmune interactomes of pain have injury-specific signatures. (a) Schematic showing the types of intercellular communication considered between immune cells and neurons for constructing the interactome. (b) Sample of the web interface for browsing evidence behind the cell-cell interactome. Each interaction is displayed as a heading summarizing the interaction ('IL6 binds IL6ST') with gene names linked to HGNC pages representing the gene. The total number of supporting pieces of evidence is shown, as is the breakdown of this number by specific source: different structured databases or literature mining systems integrated with INDRA. Each row under the heading represents a distinct database entry or sentence from a publication, with each publication linked to its corresponding PubMed

landing page. Each row also links to a curation page where feedback can be given on the correctness of the interaction. (c) Overview of the condition-specific interactome construction. The general cell-cell interactome was provided as input to Cellchat together with data from immune cells for each of the three pain conditions: UVB, Zymosan, or incision, and combined with naïve DRG neuron data. This results in three condition-specific neuroimmune interactomes. (d) The modalities of interactions and the example of INDRA-based literature evidence, as shown by PMIDs for the representative interactions, are shown in Fig. 4d. (e) Dot plots showing examples of interactions between immune cells and DRG neurons that are shared or injury-specific.



Extended Data Fig. 7 | Immune cell – DRG neurons interactome show injury-specific signatures. Heatmap of the interaction strength between immune cells (senders) and neurons (receivers) calculated for zymosan, incision and UV burn at CL, 4 h, 24 and 48 h. Color saturation represents the communication probability between the senders and receivers calculated by CellChat.



Extended Data Fig. 8 | Human TSP-1 inhibits PKA activity in human sensory neurons. (a) Box plot of *Ptgs2* and *Thbs1* expression showing normalized expression of the two genes. Upregulation of *Thbs1* mirrors pain hypersensitivity as observed in Fig. 1a. The p-values and correlation coefficients indicated below are calculated using the Pearson correlation analysis for the average expression *Thbs1* and *Ptgs2* at each timepoint per condition. (b) Timeline of iPSC-derived sensory neuron differentiation, viral transduction and experimental treatments. (c) Representative images of iPSC-derived sensory neurons expressing PKA reporter (green) treated with DMSO, forskolin (FSK), or FSK + TSP1. The scale

bar is 100 μm . Representative of two independent experiments with at least 9 wells in each condition. (d) Box plot graph showing the fold change (post/pre-treatment) in fluorescent intensity of PKA reporter in cells treated with FSK alone or FSK in the presence of escalating doses of TSP1. DMSO, $n = 9$; FSK, $n = 18$; TSP1 0.16 $\mu\text{g/ml}$, $n = 9$; TSP1 0.5 $\mu\text{g/ml}$, $n = 9$; TSP1 1.5 $\mu\text{g/ml}$, $n = 9$; TSP1 3 $\mu\text{g/ml}$, $n = 9$; TSP1 5 $\mu\text{g/ml}$, $n = 9$; TSP1 10 $\mu\text{g/ml}$, $n = 9$. Bounds of box and whiskers are 25% and 75% percentile with 95% confidence level. One-way ANOVA was performed ($n = 3$ independent experiments), ** $p < 0.005$, *** $p < 0.001$, **** $p < 0.0001$.

Reporting Summary

Nature Portfolio wishes to improve the reproducibility of the work that we publish. This form provides structure for consistency and transparency in reporting. For further information on Nature Portfolio policies, see our [Editorial Policies](#) and the [Editorial Policy Checklist](#).

Statistics

For all statistical analyses, confirm that the following items are present in the figure legend, table legend, main text, or Methods section.

n/a Confirmed

- The exact sample size (n) for each experimental group/condition, given as a discrete number and unit of measurement
- A statement on whether measurements were taken from distinct samples or whether the same sample was measured repeatedly
- The statistical test(s) used AND whether they are one- or two-sided
Only common tests should be described solely by name; describe more complex techniques in the Methods section.
- A description of all covariates tested
- A description of any assumptions or corrections, such as tests of normality and adjustment for multiple comparisons
- A full description of the statistical parameters including central tendency (e.g. means) or other basic estimates (e.g. regression coefficient) AND variation (e.g. standard deviation) or associated estimates of uncertainty (e.g. confidence intervals)
- For null hypothesis testing, the test statistic (e.g. F , t , r) with confidence intervals, effect sizes, degrees of freedom and P value noted
Give P values as exact values whenever suitable.
- For Bayesian analysis, information on the choice of priors and Markov chain Monte Carlo settings
- For hierarchical and complex designs, identification of the appropriate level for tests and full reporting of outcomes
- Estimates of effect sizes (e.g. Cohen's d , Pearson's r), indicating how they were calculated

Our web collection on [statistics for biologists](#) contains articles on many of the points above.

Software and code

Policy information about [availability of computer code](#)

Data collection

Source code to generate the interactome and the interactome gene lists used in this study are available at https://github.com/gyorilab/neuroimmune_interactome.

Data analysis

Statistical analysis, including animal numbers (n) and p values, are included in the figure legends. Statistical analysis was performed using Graphpad Prism 9. All single-cell sequencing analysis was performed using R version 4.2.3. The web resource used to present our data <http://painseq.shinyapps.io/immune/> was built using R shiny apps and Shiny Cell42.

For manuscripts utilizing custom algorithms or software that are central to the research but not yet described in published literature, software must be made available to editors and reviewers. We strongly encourage code deposition in a community repository (e.g. GitHub). See the Nature Portfolio [guidelines for submitting code & software](#) for further information.

Data

Policy information about [availability of data](#)

All manuscripts must include a [data availability statement](#). This statement should provide the following information, where applicable:

- Accession codes, unique identifiers, or web links for publicly available datasets
- A description of any restrictions on data availability
- For clinical datasets or third party data, please ensure that the statement adheres to our [policy](#)

Raw immune cell scRNA-seq files from healthy and injured skin samples will be deposited at the Gene Expression Omnibus repository (GEO) with a GEO accession

number (GSE255686). The analyzed dataset from immune cell scRNA seq is also available on <http://painseq.shinyapps.io/immune/>. Source code to generate the interactome and the interactome gene lists used in this study is available at: https://github.com/gyorilab/neuroimmune_interactome.

Research involving human participants, their data, or biological material

Policy information about studies with [human participants or human data](#). See also policy information about [sex, gender \(identity/presentation\), and sexual orientation](#) and [race, ethnicity and racism](#).

Reporting on sex and gender	<input type="text" value="N/A"/>
Reporting on race, ethnicity, or other socially relevant groupings	<input type="text" value="N/A"/>
Population characteristics	<input type="text" value="N/A"/>
Recruitment	<input type="text" value="N/A"/>
Ethics oversight	<input type="text" value="N/A"/>

Note that full information on the approval of the study protocol must also be provided in the manuscript.

Field-specific reporting

Please select the one below that is the best fit for your research. If you are not sure, read the appropriate sections before making your selection.

Life sciences Behavioural & social sciences Ecological, evolutionary & environmental sciences

For a reference copy of the document with all sections, see [nature.com/documents/nr-reporting-summary-flat.pdf](https://www.nature.com/documents/nr-reporting-summary-flat.pdf)

Life sciences study design

All studies must disclose on these points even when the disclosure is negative.

Sample size	<input type="text" value="Sample size for behavioral experiments was based on previous data in the lab. Sample size for scRNA seq experiment was based on what is established in the field at n=2 for single cell transcriptomics. No statistical methods were used to pre-determine sample sizes but our sample sizes are similar to those reported in previous publications (zhang et. al., 2022)."/>
Data exclusions	<input type="text" value="No data was excluded"/>
Replication	<input type="text" value="All attempts at replication were successful. The replication number for each experiment is included in the legends."/>
Randomization	<input type="text" value="For behavior experiments, mice were chosen randomly from each cage. For Ca imaging experiments, dishes with DRG cultures were chosen randomly for treatment groups."/>
Blinding	<input type="text" value="For behavior experiments, person inducing the stimulus was different from the person investigating the behavior who was fully blinded."/>

Reporting for specific materials, systems and methods

We require information from authors about some types of materials, experimental systems and methods used in many studies. Here, indicate whether each material, system or method listed is relevant to your study. If you are not sure if a list item applies to your research, read the appropriate section before selecting a response.

Materials & experimental systems

n/a	Involvement
<input type="checkbox"/>	<input checked="" type="checkbox"/> Antibodies
<input type="checkbox"/>	<input checked="" type="checkbox"/> Eukaryotic cell lines
<input checked="" type="checkbox"/>	<input type="checkbox"/> Palaeontology and archaeology
<input type="checkbox"/>	<input checked="" type="checkbox"/> Animals and other organisms
<input checked="" type="checkbox"/>	<input type="checkbox"/> Clinical data
<input checked="" type="checkbox"/>	<input type="checkbox"/> Dual use research of concern
<input checked="" type="checkbox"/>	<input type="checkbox"/> Plants

Methods

n/a	Involvement
<input checked="" type="checkbox"/>	<input type="checkbox"/> ChIP-seq
<input type="checkbox"/>	<input checked="" type="checkbox"/> Flow cytometry
<input checked="" type="checkbox"/>	<input type="checkbox"/> MRI-based neuroimaging

Antibodies

Antibodies used	All antibodies used in this study were specific to mice. Flow cytometry antibodies include CD45-FITC (1:400, Biolegend, Cat no.103107), CD64-PE-594 (1:600, Biolegend, Cat no. 139319), CD11c-APC (1:400, Biolegend, 101211) Cd11b- eFluor 780 (1:400, ebioscience, 47-0112-82), Ly6G-PE(1:800, Biolegend, 127607) and Ly6c-BV711 (1:2000, Biolegend, 128037). IHC antibodies include (Rb anti-PGP9.5 abcam ab108986 1:500, Goat anti-CD47 RnD Systems AF1866 1:200), (Donkey anti-Rb Cy3 Jackson ImmunoResearch 711-165-152 1:500, Donkey anti-Goat 647 Thermo Fischer A-21447 1:500).
Validation	All antibodies have been validated by manufacturer.

Eukaryotic cell lines

Policy information about [cell lines and Sex and Gender in Research](#)

Cell line source(s)	IPSC lines were obtained from Lonza iPS (LiPS.GR-1-1). This cell line was derived from a male donor.
Authentication	No authentication was performed.
Mycoplasma contamination	No mycoplasma contamination was detected.
Commonly misidentified lines (See ICLAC register)	N/A

Animals and other research organisms

Policy information about [studies involving animals; ARRIVE guidelines](#) recommended for reporting animal research, and [Sex and Gender in Research](#)

Laboratory animals	Both Male and Female mice were used in all the behavior experiments. Single-cell RNA sequencing was performed on 8 wks old female mice. 8-12-week-old C57BL/6J mice were obtained from the Jackson Laboratory (JAX:000664) as were Cd47 deficient mice (Jax:003173). All mice in this study were kept on a 12h light cycle, at 21–23°C, with 30–50% humidity.
Wild animals	No Wild animals were used.
Reporting on sex	All the information on sex used in individual experiments is included in the text.
Field-collected samples	Please state here that no field collected samples were used in the study.
Ethics oversight	All animal experiments were conducted according to institutional animal care and safety guidelines at Boston Children's Hospital and Harvard Medical School

Note that full information on the approval of the study protocol must also be provided in the manuscript.

Flow Cytometry

Plots

Confirm that:

- The axis labels state the marker and fluorochrome used (e.g. CD4-FITC).
- The axis scales are clearly visible. Include numbers along axes only for bottom left plot of group (a 'group' is an analysis of identical markers).
- All plots are contour plots with outliers or pseudocolor plots.
- A numerical value for number of cells or percentage (with statistics) is provided.

Methodology

Sample preparation	The planter skin of the mouse hind paw was dissected, separating the muscle and collected into 1% BSA containing RPMI. The skin was minced using scissors into 1-2mm pieces. Liberase TM (Roche) was added to the media at a final concentration of 0.5 mg/ml. Tissue was digested at 37c while vortexing at 1000rpm for 90 min.
Instrument	The digested tissue was strained using a 100uM strainer to obtain a single-cell suspension used for flow sorting on BD ArialI and single cell transcriptomics.
Software	Analysis software FlowJo 10
Cell population abundance	Cell abundance is shown in Supp Fig 2 and quantified in Fig 1F. Purity was determined by postsort analysis. The post sort data is not included since these cells were used for single cell RNA seq for which non-CD45+ populations are indicated.

Gating strategy

Gating strategy for immune cell sorting is shown in Supp Fig 1A. Gating strategy for myeloid cells is shown in Supp Fig 2A.

Tick this box to confirm that a figure exemplifying the gating strategy is provided in the Supplementary Information.